

# Residual zonal flows in tokamaks and stellarators at arbitrary wavelengths

**Pedro Monreal**<sup>1</sup>

E-mail: pedro.monreal@ciemat.es

**Iván Calvo**<sup>1</sup>

E-mail: ivan.calvo@ciemat.es

**Edilberto Sánchez**<sup>1</sup>

E-mail: edi.sanchez@ciemat.es

**Félix I Parra**<sup>2,3</sup>

E-mail: felix.parradiatz@physics.ox.ac.uk

**Andrés Bustos**<sup>4,5</sup>

E-mail: anbustos@fis.uc3m.es

**Axel Könies**<sup>6</sup>

E-mail: axel.koenies@ipp.mpg.de

**Ralf Kleiber**<sup>6</sup>

E-mail: ralf.kleiber@ipp.mpg.de

**Tobias Görler**<sup>4</sup>

E-mail: tbg@ipp.mpg.de

<sup>1</sup>Laboratorio Nacional de Fusión, CIEMAT, 28040 Madrid, Spain

<sup>2</sup>Rudolf Peierls Centre for Theoretical Physics, University of Oxford, Oxford, OX1 3NP, UK

<sup>3</sup>Culham Centre for Fusion Energy, Abingdon, OX14 3DB, UK

<sup>4</sup>Max-Planck-Institut für Plasmaphysik, D-85748 Garching, Germany

<sup>5</sup>Departamento de Física, Universidad Carlos III de Madrid, 28911 Leganés, Spain

<sup>6</sup>Max-Planck-Institut für Plasmaphysik, D-17491 Greifswald, Germany

April 9, 2018

**Abstract.** In the linear collisionless limit, a zonal potential perturbation in a toroidal plasma relaxes, in general, to a non-zero residual value. Expressions for the residual value in tokamak and stellarator geometries, and for arbitrary wavelengths, are derived. These expressions involve averages over the lowest order particle trajectories, that typically cannot be evaluated analytically. In this work, an efficient numerical method for the evaluation of such expressions is reported. It is shown that this method is faster than direct gyrokinetic simulations performed with the GENE and EUTERPE codes. Calculations of the residual value in stellarators are provided for much shorter wavelengths than previously available in the literature. Electrons must be treated kinetically in stellarators because, unlike in tokamaks, kinetic electrons modify the residual value even at long wavelengths. This effect, that had already been predicted theoretically, is confirmed by gyrokinetic simulations.

## 1. Introduction

Whereas the reduction of turbulent transport by zonal flows is a widely accepted phenomenon [1, 2], its quantitative understanding is still poor. The determination of the zonal flow amplitude and turbulent transport level are nonlinear questions whose answers require costly gyrokinetic simulations. The cost grows enormously if, by means of parameter scans, one wants to know how those quantities depend on the magnetic geometry or the plasma conditions. A useful simplification is provided by the initial value problem consisting of calculating the long-time and collisionless evolution of a zonal perturbation. Among other reasons, its usefulness is due to the fact that an exact expression for the value of the perturbation at  $t = \infty$ , called residual value, can be derived. Even though the explicit evaluation of the final expression can only be carried out in simplified geometries and for long wavelengths of the perturbation, the analytical solution gives insight into the physics. This partly explains the attention attracted by the work of Rosenbluth and Hinton [3] and the effort put on subsequent extensions that we cite below. In stellarator research, the interest in this problem was spurred by the suggestion [4] of a direct relation between zonal flow residual value and turbulent transport level.

The seminal paper [3] dealt with long-wavelength potential perturbations in large aspect ratio and circular cross section tokamaks. Explicit solutions of related problems for more complex tokamak geometries and arbitrary wavelengths have been given in [5, 6]. In recent years, several articles have addressed the problem in stellarators [7, 8, 9, 10, 11]. In this paper we report on a code to evaluate fast and accurately the exact expressions of the zonal flow residual value, for arbitrary wavelengths and for tokamak and stellarator geometries. But why is this useful if the same answer can be obtained, in principle, by linear runs of a local gyrokinetic code? As we will illustrate later on, it turns out that the solution by means of gyrokinetic simulations of the residual zonal flow problem, especially at short wavelengths, is very demanding in terms of computational resources. We will show that our method is faster. These differences can be of several orders of magnitude in computing time, especially in the case of stellarators. Moreover, the code and the results of this work are not only interesting from the point of view of physics, but also for validation of gyrokinetic codes.

The rest of the paper is organized as follows. In Section 2 we derive the residual zonal flow expressions for arbitrary wavelengths and magnetic geometry. In Section 3 we report on the code used to evaluate the expressions presented in Section 2. As a check, we compare our calculations with analytical results from [5, 6], obtained in simplified tokamak geometry. In order to avoid any confusion, we note that the results in [5, 6] were not derived as an initial value problem, but as the stationary solution of a forced system. We explain this in more detail in Section 3. In Section 4 our results are compared with local and global gyrokinetic simulations of the initial value problem, employing the codes GENE [12, 13, 14, 15] and EUTERPE [16, 17], respectively. We also compare the differences in computational time required by each approach showing

that the method introduced in this paper is faster than those gyrokinetic simulations. Stellarator residual values are calculated, using our method and also gyrokinetic codes, for a range of wavelengths much wider than previously available in the literature. The stellarator calculations are done for the standard configuration of Wendelstein 7-X (W7-X). We comment on a purely stellarator effect already predicted in [8, 10]; namely, that the approximation of adiabatic electrons is always incorrect (even at long wavelengths) for the purpose of determining the residual zonal flow in stellarators. We quantify the error by computing, with our method, the residual value when kinetic or adiabatic electrons are used. This result is confirmed by gyrokinetic simulations. The conclusions are presented in Section 5.

Throughout this paper, we assume that the electrostatic potential  $\varphi$  associated to the zonal flow is constant on flux surfaces. It is true that zonal flows (*i.e.* flows that are only weakly damped, and therefore remain in the plasma for long times) usually correspond to electrostatic potentials with small variations on flux surfaces, but we should emphasize that assuming that  $\varphi$  is constant on flux surfaces is, at most, a good approximation.

## 2. Linear collisionless evolution of zonal flows

In this section, we give a detailed calculation of the residual zonal flow for arbitrary wavelengths in tokamak and stellarator geometries. We solve the linear and collisionless gyrokinetic equations at long times, assuming that the electrostatic potential perturbation is constant on flux surfaces.

In strongly magnetized plasmas, one employs the smallness of  $\rho_{ts^*} = \rho_{ts}/L$  to average over the gyromotion. Here,  $L$  is the characteristic length of variation of the magnitude of the magnetic field  $B$ ,  $\rho_{ts} = v_{ts}/\Omega_s$  is the thermal gyroradius,  $v_{ts} = \sqrt{T_s/m_s}$  is the thermal speed,  $\Omega_s = Z_s e B/m_s$  is the gyrofrequency,  $T_s$  is the equilibrium temperature,  $m_s$  is the mass, and  $Z_s e$  is the charge of species  $s$ , where  $e$  is the proton charge. Gyrokinetic theory [18, 19, 20, 21, 22, 23] gives a procedure to rigorously derive the gyroaveraged kinetic equations order by order in  $\rho_{ts^*} \ll 1$ . The averaging operation is conveniently expressed in a new set of phase space coordinates, called gyrokinetic coordinates. Denote by  $\{\mathbf{r}, \mathbf{v}\}$  the particle position and velocity. The coordinate transformation, to lowest order in  $\rho_{ts^*}$ , is given by

$$\begin{aligned} \mathbf{r} &= \mathbf{R} + \boldsymbol{\rho}_s(\mathbf{R}, v, \lambda, \gamma) + O(\rho_{ts^*}^2 L), \\ \mathbf{v} &= v_{\parallel}(\mathbf{R}, v, \lambda, \sigma) \hat{\mathbf{b}}(\mathbf{R}) + \Omega_s \boldsymbol{\rho}_s(\mathbf{R}, v, \lambda, \gamma) \times \hat{\mathbf{b}}(\mathbf{R}) + O(\rho_{ts^*} v_{ts}). \end{aligned} \quad (1)$$

In equation (1),  $\mathbf{R}$  is the gyrocenter position,  $v$  is the magnitude of  $\mathbf{v}$ ,  $\lambda = B^{-1} v_{\perp}^2 / v^2$  is the pitch angle,  $\sigma = v_{\parallel} / |v_{\parallel}|$  is the sign of the parallel velocity

$$v_{\parallel}(\mathbf{R}, v, \lambda, \sigma) = \sigma v \sqrt{1 - \lambda B(\mathbf{R})}, \quad (2)$$

$\hat{\mathbf{b}}$  is the unit vector in the direction of the magnetic field  $\mathbf{B}$ ,  $v_{\perp}$  is the component of the

velocity perpendicular to  $\mathbf{B}$ , and  $\boldsymbol{\rho}_s$  is the gyroradius vector, defined as

$$\boldsymbol{\rho}_s(\mathbf{R}, v, \lambda, \gamma) = \frac{m_s v}{Z_s e} \sqrt{\frac{\lambda}{B(\mathbf{R})}} [\hat{\mathbf{e}}_2(\mathbf{R}) \cos \gamma - \hat{\mathbf{e}}_1(\mathbf{R}) \sin \gamma]. \quad (3)$$

Here,  $\hat{\mathbf{e}}_1(\mathbf{R})$  and  $\hat{\mathbf{e}}_2(\mathbf{R})$  are unit vector fields orthogonal to each other which satisfy  $\hat{\mathbf{e}}_1 \times \hat{\mathbf{e}}_2 = \hat{\mathbf{b}}$  at every point. Finally, the gyrophase  $\gamma$  is

$$\gamma = \arctan(\mathbf{v} \cdot \hat{\mathbf{e}}_2 / \mathbf{v} \cdot \hat{\mathbf{e}}_1). \quad (4)$$

We introduce straight field line coordinates  $\{\psi, \theta, \zeta\}$ , where  $\psi \in [0, 1]$  is the radial coordinate defined as the normalized toroidal flux  $\psi = \Psi_t / \Psi_t^{\text{edge}}$ ,  $\theta$  is a poloidal angle and  $\zeta$  is a toroidal angle, with  $\theta, \zeta \in [0, 1)$ . The magnetic field in these coordinates is written as

$$\mathbf{B} = -\Psi_p'(\psi) \nabla \psi \times \nabla (\zeta - q(\psi) \theta). \quad (5)$$

Here,  $q(\psi) = \Psi_t'(\psi) / \Psi_p'(\psi)$  is the safety factor, and  $\Psi_p'(\psi)$  and  $\Psi_t'(\psi)$  are the derivatives of the poloidal and toroidal fluxes with respect to  $\psi$ . It will be convenient to define the coordinate  $\alpha := \zeta - q(\psi) \theta$ , that labels magnetic field lines on each flux surface. Unless otherwise stated, we use  $\{\psi, \theta, \alpha\}$  as the set of independent spatial coordinates. Note that  $\mathbf{B} \cdot \nabla \psi = 0$ ,  $\mathbf{B} \cdot \nabla \alpha = 0$ . We employ  $\theta$  as the coordinate along a field line.

The distribution function in gyrokinetic coordinates,  $F_s = F_s(\psi, \theta, \alpha, v, \lambda, \sigma, \gamma, t)$ , can be written as

$$F_s(\mathbf{R}, v, \lambda, \sigma, \gamma, t) = F_{s0}(\mathbf{R}, v) + F_{s1}(\mathbf{R}, v, \lambda, \sigma, t) + O(\rho_{ts}^2 F_{s0}), \quad (6)$$

where  $F_{s1} = O(\rho_{ts} F_{s0})$  and  $F_{s0}$  is a Maxwellian distribution whose density  $n_s$  and temperature  $T_s = m_s v_{ts}^2$  are flux functions,

$$F_{s0}(\mathbf{R}, v) := \frac{n_s(\psi(\mathbf{R}))}{(\sqrt{2\pi} v_{ts}(\psi(\mathbf{R})))^3} \exp\left(-\frac{v^2}{2v_{ts}^2(\psi(\mathbf{R}))}\right). \quad (7)$$

The lowest-order quasineutrality condition implies  $\sum_s Z_s e n_s(\psi) = 0$ . Note that to  $O(\rho_{ts} F_{s0})$  the distribution function is independent of the gyrophase.

The linear and collisionless time evolution of  $F_{s1}$  is given by [24, 23]

$$\begin{aligned} \partial_t H_{s1} + (v_{\parallel} \hat{\mathbf{b}} + \mathbf{v}_{ds}) \cdot \nabla H_{s1} &= \frac{Z_s e}{T_s} \partial_t \langle \varphi \rangle F_{s0} \\ &+ \frac{1}{B} \left( \nabla \langle \varphi \rangle \times \hat{\mathbf{b}} \right) \cdot \nabla \psi \left[ \frac{n_s'}{n_s} + \left( \frac{m_s v^2}{2T_s} + \frac{3}{2} \right) \frac{T_s'}{T_s} \right] F_{s0}, \end{aligned} \quad (8)$$

where primes denote differentiation with respect to  $\psi$ , the function  $H_{s1}$  is defined by

$$H_{s1} = F_{s1} + \frac{Z_s e}{T_s} \langle \varphi \rangle F_{s0}, \quad (9)$$

the gyroaveraged electrostatic potential is

$$\langle \varphi \rangle(\mathbf{R}, v, \lambda, t) := \frac{1}{2\pi} \int_0^{2\pi} \varphi(\mathbf{R} + \boldsymbol{\rho}_s(\mathbf{R}, v, \lambda, \gamma), t) d\gamma \quad (10)$$

and the magnetic drift velocity reads

$$\mathbf{v}_{ds} = \frac{v^2}{\Omega_s} \hat{\mathbf{b}} \times \left[ (1 - \lambda B) \hat{\mathbf{b}} \cdot \nabla \hat{\mathbf{b}} + \frac{\lambda}{2} \nabla B \right]. \quad (11)$$

The orderings in gyrokinetic theory allow to separate the variations of the fields on the small and large scales, and decompose in Fourier modes with respect to the former. Since we are interested in studying the evolution of an electrostatic potential perturbation that depends only on  $\psi$  and the problem is linear, we can take a single mode of the form

$$\varphi(\mathbf{r}, t) = \varphi_k(\psi(\mathbf{r}), t) \exp(ik_\psi \psi(\mathbf{r})). \quad (12)$$

Here,

$$L^{-1} \ll k_\perp \lesssim \rho_{ts}^{-1} \quad (13)$$

with  $k_\perp(\mathbf{R}) = k_\psi |\nabla \psi(\mathbf{R})|$ , and  $\varphi_k$  varies on the macroscopic scale  $L$ . Observe that, due to the effects of magnetic geometry, the dependence of  $\varphi_k$  on  $\psi$  cannot be avoided even for flat density and temperature profiles. A recent explanation of scale separation, as well as a proof of the equivalence between the local and global approaches to gyrokinetic theory can be found in [25].

To lowest order, the gyroaveraged electrostatic potential is

$$\langle \varphi \rangle(\mathbf{R}, v, \lambda, t) = \varphi_k(\psi(\mathbf{R}), t) J_0(k_\perp \rho_s) \exp(ik_\psi \psi(\mathbf{R})), \quad (14)$$

where the magnitude of the gyroradius vector is

$$\rho_s(\mathbf{R}, v, \lambda) = \frac{m_s v}{Z_s e} \sqrt{\frac{\lambda}{B(\mathbf{R})}} \quad (15)$$

and  $J_0$  is the zeroth-order Bessel function of the first kind,

$$J_0(x) = \frac{1}{2\pi} \int_0^{2\pi} \exp(ix \sin \gamma) d\gamma. \quad (16)$$

If the electrostatic potential has the form (12), then the distribution function can be written as

$$F_{s1}(\mathbf{R}, v, \lambda, \sigma, t) = f_s(\psi(\mathbf{R}), \theta(\mathbf{R}), \alpha(\mathbf{R}), v, \lambda, \sigma, t) \exp(ik_\psi \psi(\mathbf{R})) \quad (17)$$

and consequently

$$H_{s1}(\mathbf{R}, v, \lambda, \sigma, t) = h_s(\psi(\mathbf{R}), \theta(\mathbf{R}), \alpha(\mathbf{R}), v, \lambda, \sigma, t) \exp(ik_\psi \psi(\mathbf{R})), \quad (18)$$

where  $f_s$  and  $h_s$  vary on the scale  $L$ . Then, equation (8) becomes

$$\left( \partial_t + v_\parallel \hat{\mathbf{b}} \cdot \nabla + ik_\psi \omega_s \right) h_s = \frac{Z_s e}{T_s} \partial_t \varphi_k J_0 F_{s0}, \quad (19)$$

where we have used the notation  $\omega_s := \mathbf{v}_{ds} \cdot \nabla \psi$  for the radial magnetic drift frequency and  $J_{0s} \equiv J_0(k_\perp \rho_s)$ . From now on, and for brevity, we omit the dependence of  $\varphi_k$  on  $\psi$ ; that is, we write  $\varphi_k(t)$  instead of  $\varphi_k(\psi, t)$ .

Denote by  $\omega$  the frequency associated to the time derivative in (19). The objective is to expand (19) in powers of  $\omega/(v_{ts} L^{-1}) \ll 1$ , solve the lowest order equations and

determine  $\varphi_k(t)$  in the limit  $t \rightarrow \infty$ . The  $\omega/(v_{ts}L^{-1}) \ll 1$  expansion means, in particular, that we average over the lowest order particle trajectories and solve for time scales much longer than a typical orbit time, which is  $O(L/v_{ts})$ . We define the orbit average for a phase-space function  $Q(\psi, \theta, \alpha, v, \lambda, \sigma, t)$  as

$$\overline{Q} := \begin{cases} \langle BQ/|v_{\parallel}| \rangle_{\psi} / \langle B/|v_{\parallel}| \rangle_{\psi} & \text{for passing particles} \\ \omega_b \oint d\theta Q / (v_{\parallel} \hat{\mathbf{b}} \cdot \nabla \theta) & \text{for trapped particles,} \end{cases} \quad (20)$$

where  $\omega_b := [\oint d\theta / (v_{\parallel} \hat{\mathbf{b}} \cdot \nabla \theta)]^{-1}$  is the bounce frequency. Given a function  $G(\psi, \theta, \alpha)$ , the flux surface average is defined by

$$\langle G \rangle_{\psi} = V'(\psi)^{-1} \int_0^1 d\theta \int_0^1 d\alpha \sqrt{g} G(\psi, \theta, \alpha). \quad (21)$$

Here,  $\sqrt{g} = [(\nabla\psi \times \nabla\theta) \cdot \nabla\alpha]^{-1}$  is the square root of the metric determinant and  $V'(\psi) = \int_0^1 d\theta \int_0^1 d\alpha \sqrt{g}$  is the derivative of the volume enclosed by the flux surface labeled by  $\psi$ . The symbol  $\oint$  stands for integration over the trapped trajectory, where the bounce points  $\theta_b$  are the solutions of  $1 - \lambda B(\psi, \theta_b, \alpha) = 0$  for given values of  $\psi$  and  $\alpha$ , and given an initial condition for the particle trajectory.

Observe that the orbit average operation has the property

$$\overline{v_{\parallel} \hat{\mathbf{b}} \cdot \nabla Q} = 0 \quad (22)$$

for any single-valued function  $Q$ . We write the radial magnetic drift frequency as a sum of its orbit averaged and fluctuating parts

$$\omega_s = \overline{\omega_s} + v_{\parallel} \hat{\mathbf{b}} \cdot \nabla \delta_s, \quad (23)$$

where  $\delta_s = \delta_s(\psi, \theta, \alpha, v, \lambda, \sigma)$ , that we choose to be odd in  $\sigma$ , is the radial displacement of the particle's gyrocenter from its mean flux surface. The solution of the magnetic differential equation that determines  $\delta_s$  is given in [Appendix A](#).

Defining  $\underline{h}_s := h_s \exp(ik_{\psi}\delta_s)$  and  $\underline{\varphi}_k := \varphi_k \exp(ik_{\psi}\delta_s)$ , equation (19) yields

$$\left( \partial_t + v_{\parallel} \hat{\mathbf{b}} \cdot \nabla + ik_{\psi} \overline{\omega_s} \right) \underline{h}_s = \frac{Z_s e}{T_s} \partial_t \underline{\varphi}_k J_{0s} F_{s0}. \quad (24)$$

It is worth noting that the expansion in  $\omega/(v_{ts}L^{-1})$  only makes sense if

$$\frac{k_{\psi} \overline{\omega_s}}{v_{ts}L^{-1}} \sim \frac{\omega}{v_{ts}L^{-1}} \ll 1. \quad (25)$$

For  $k_{\perp} \rho_{ts} \sim 1$ , this implies

$$\frac{\overline{\omega_s}}{\omega_s} \sim \frac{\omega}{v_{ts}L^{-1}} \ll 1. \quad (26)$$

This trivially holds in a tokamak because  $\overline{\omega_s} = 0$  for all trajectories. In a generic stellarator,  $\overline{\omega_s} = 0$  only for passing particles. Then, condition (26) requires that the secular radial drifts of trapped particles be sufficiently small. We assume that this is the case and carry out the expansion in  $\omega/(v_{ts}L^{-1})$ .

We write

$$\underline{h}_s = \underline{h}_s^{(0)} + \underline{h}_s^{(1)} + \underline{h}_s^{(2)} + \dots, \quad (27)$$

with  $\underline{h}_s^{(j+1)}/\underline{h}_s^{(j)} \sim \omega/(v_{ts}L^{-1})$ . Then, we expand equation (24). To lowest order, one obtains

$$v_{\parallel} \hat{\mathbf{b}} \cdot \nabla \underline{h}_s^{(0)} = 0, \quad (28)$$

implying that  $\underline{h}_s^{(0)}$  is constant along the lowest order trajectories; *i.e.*

$$\underline{h}_s^{(0)} = \overline{h_s^{(0)}}. \quad (29)$$

To next order, we have

$$(\partial_t + ik_{\psi} \overline{\omega_s}) \underline{h}_s^{(0)} + v_{\parallel} \hat{\mathbf{b}} \cdot \nabla \underline{h}_s^{(1)} = \frac{Z_s e}{T_s} \partial_t \underline{\varphi}_k J_{0s} F_{s0}. \quad (30)$$

We do not write  $\underline{\varphi}_k^{(0)}$  to ease the notation. The orbit average of (30) annihilates the term  $v_{\parallel} \hat{\mathbf{b}} \cdot \nabla \underline{h}_s^{(1)}$ , and we find

$$(\partial_t + ik_{\psi} \overline{\omega_s}) \underline{h}_s^{(0)} = \frac{Z_s e}{T_s} \overline{\partial_t \underline{\varphi}_k J_{0s} F_{s0}}. \quad (31)$$

It is useful to work in Laplace space in order to solve this equation. The Laplace transform of a function  $Q(t)$  is defined as  $\widehat{Q}(p) = \int_0^{\infty} Q(t) e^{-pt} dt$ , where  $p$  denotes the variable in Laplace space. We apply it to (31) and obtain

$$(p + ik_{\psi} \overline{\omega_s}) \widehat{\underline{h}}_s^{(0)} = \frac{Z_s e}{T_s} p \overline{\widehat{\underline{\varphi}}_k J_{0s} F_{s0}} + \underline{f}_s(0). \quad (32)$$

Here,  $\underline{f}_s(0) := f_s(0) \exp(ik_{\psi} \delta_s)$  and  $f_s(0)$  is the initial condition for  $f_s$ ; *i.e.*  $f_s(0) \equiv f_s(\psi, \theta, \alpha, v, \lambda, \sigma, 0)$ .

The solution of (32) yields

$$\widehat{\underline{h}}_s^{(0)} = \frac{e^{-ik_{\psi} \delta_s}}{p + ik_{\psi} \overline{\omega_s}} \left( \frac{Z_s e}{T_s} p \overline{\widehat{\underline{\varphi}}_k e^{ik_{\psi} \delta_s} J_{0s} F_{s0}} + e^{ik_{\psi} \delta_s} f_s(0) \right). \quad (33)$$

In order to have a closed system of equations we employ the gyrokinetic quasineutrality equation (see, for example, references [24, 23]),

$$\sum_s \frac{Z_s^2 e}{T_s} n_s \varphi(\mathbf{R}, t) = \sum_s Z_s \int H_s(\mathbf{R} - \boldsymbol{\rho}_s(\mathbf{R}, v, \lambda, \gamma), v, \lambda, \sigma, t) d^3 v. \quad (34)$$

Here, the short-hand notation  $\int Q d^3 v$  means, for a function  $Q(\psi, \theta, \alpha, v, \lambda, \sigma, \gamma)$ ,

$$\int Q d^3 v = \sum_{\sigma=-1}^1 \int_0^{2\pi} d\gamma \int_0^{\infty} dv \int_0^{1/B} d\lambda \frac{v^2 B}{2\sqrt{1-\lambda B}} Q(\psi, \theta, \alpha, v, \lambda, \sigma, \gamma). \quad (35)$$

Using (12) and (18), and flux-surface averaging, we get

$$\sum_s \frac{Z_s^2 e}{T_s} n_s \varphi_k = \left\langle \sum_s Z_s \int J_{0s} h_s d^3 v \right\rangle_{\psi}. \quad (36)$$

To lowest order in  $\omega/(v_{ts}L^{-1}) \ll 1$ , and after transforming to Laplace space, equation (36) gives

$$\sum_s \frac{Z_s^2 e}{T_s} n_s \widehat{\varphi}_k = \left\langle \sum_s Z_s \int J_{0s} \widehat{h}_s^{(0)} d^3v \right\rangle_\psi. \quad (37)$$

We employ (33) to write the right side of (37) in terms of the electrostatic potential and the initial condition, and solve for  $\widehat{\varphi}_k$ . The result is

$$\widehat{\varphi}_k(p) = \frac{\sum_s Z_s \left\{ \frac{1}{p + ik_\psi \overline{\omega}_s} e^{-ik_\psi \delta_s} J_{0s} \overline{e^{ik_\psi \delta_s} f_s(0)} / F_{s0} \right\}_s}{\sum_s \frac{Z_s^2 e}{T_s} \left\{ 1 - \frac{p}{p + ik_\psi \overline{\omega}_s} e^{-ik_\psi \delta_s} J_{0s} \overline{e^{ik_\psi \delta_s} J_{0s}} \right\}_s}, \quad (38)$$

where we have simplified the notation by defining

$$\{Q\}_s := \left\langle \sum_{\sigma=-1}^1 \int_0^\infty dv \int_0^{1/B} d\lambda \frac{\pi v^2 B}{\sqrt{1 - \lambda B}} Q(\psi, \theta, \alpha, v, \lambda, \sigma) F_{s0} \right\rangle_\psi \quad (39)$$

for gyrophase independent functions on phase space.

The residual value is found from the well-known property of the Laplace transform

$$\lim_{t \rightarrow \infty} \varphi_k(t) = \lim_{p \rightarrow 0} p \widehat{\varphi}_k(p). \quad (40)$$

Applying (40) to equation (38), we find

$$\varphi_k(\infty) = \frac{\sum_s Z_s \left\{ e^{-ik_\psi \delta_s} J_{0s} \overline{e^{ik_\psi \delta_s} f_s(0)} / F_{s0} \right\}_s^{\overline{\omega}_s=0}}{\sum_s \frac{Z_s^2 e}{T_s} \left[ \{1\}_s - \left\{ e^{-ik_\psi \delta_s} J_{0s} \overline{e^{ik_\psi \delta_s} J_{0s}} \right\}_s^{\overline{\omega}_s=0} \right]}, \quad (41)$$

where  $\varphi_k(\infty) \equiv \lim_{t \rightarrow \infty} \varphi_k(t)$ . The superscript  $\overline{\omega}_s = 0$  means that the integration is performed only for particles whose trajectory satisfies  $\overline{\omega}_s = 0$ . In tokamaks, this property holds true for both trapped and passing particles, and therefore the integrals in (41) are performed over the whole phase space. In stellarators,  $\overline{\omega}_s = 0$  is satisfied exclusively for passing particles. Only in perfectly omnigenous stellarators [26, 27, 28] have trapped particles vanishing average radial magnetic drift. Hence, in a generic stellarator, the integrals in (41) with superscript  $\overline{\omega}_s = 0$  are performed only over the passing region of phase space.

The residual level is usually defined as the normalized value  $\varphi_k(\infty)/\varphi_k(0)$ . The relation between  $f_s(0)$  and  $\varphi_k(0)$  is given by the flux-surface averaged quasineutrality equation at  $t = 0$ ,

$$\sum_s \frac{Z_s^2 e}{T_s} n_s \langle 1 - \Gamma_0(k_\perp^2 \rho_{ts}^2) \rangle_\psi \varphi_k(0) = \left\langle \sum_s Z_s \int J_{0s} f_s(0) d^3v \right\rangle_\psi. \quad (42)$$

Here, we have employed the identity  $\int J_0^2(k_\perp \rho_s) F_{0s} d^3v = n_s \Gamma_0(k_\perp^2 \rho_{ts}^2)$ , where  $\Gamma_0(k_\perp^2 \rho_{ts}^2) := e^{-k_\perp^2 \rho_{ts}^2} I_0(k_\perp^2 \rho_{ts}^2)$ , and  $I_0$  is the zeroth order modified Bessel function. We will use the notation  $\Gamma_{0s} \equiv \Gamma_0(k_\perp^2 \rho_{ts}^2)$ .



For later comparison with gyrokinetic simulations, it will be useful to have at hand the expressions corresponding to the approximation of adiabatic electrons. Using this approximation, equation (36) can be written as

$$\sum_{s \neq e} \frac{Z_s^2 e}{T_s} n_s \widehat{\varphi}_k(p) = \left\langle \sum_{s \neq e} Z_s \int d^3 v J_{0s} \widehat{h}_s(p) \right\rangle_{\psi}. \quad (43)$$

Proceeding as shown previously for the fully kinetic case, we find that the expression for  $\varphi_k(\infty)$  reads

$$\varphi_k(\infty) = \frac{\sum_{s \neq e} Z_s \left\{ e^{-ik_{\psi} \delta_s} J_{0s} \overline{e^{ik_{\psi} \delta_s} f_s(0)} / F_{s0} \right\}_s^{\overline{\omega_s=0}}}{\sum_{s \neq e} \frac{Z_s^2 e}{T_s} \left[ \{1\}_s - \left\{ e^{-ik_{\psi} \delta_s} J_{0s} \overline{e^{ik_{\psi} \delta_s} J_{0s}} \right\}_s^{\overline{\omega_s=0}} \right]}. \quad (44)$$

In this case, the equation that relates  $f_s(0)$  and  $\varphi_k(0)$  is

$$\sum_{s \neq e} \frac{Z_s^2 e}{T_s} n_s \langle 1 - \Gamma_{0s} \rangle_{\psi} \varphi_k(0) = \left\langle \sum_{s \neq e} Z_s \int J_{0s} f_s(0) d^3 v \right\rangle_{\psi}. \quad (45)$$

The residual zonal flow was computed in reference [3] for  $k_{\perp} \rho_{ti} \ll 1$  in a large aspect ratio, circular cross section tokamak with adiabatic electrons. An extension of the derivation of [3] was proposed in references [5, 6] to allow for short-wavelength perturbations, and also for kinetic electrons and more complex tokamak geometries. In reference [6], comparisons of analytical calculations with gyrokinetic simulations are shown. The enhancement of tokamak residual zonal flows at short wavelengths was originally found in reference [12] by means of gyrokinetic simulations with the code GS2. But the short-wavelength calculations of [12, 5, 6] do not correspond to an initial value problem because the quasineutrality equation is forced with a source term. At long wavelengths, the initial value problem and the forced system give the same result. This will be explained in more detail in Section 3.

In stellarators, the residual zonal flow calculation has been done in [7, 8, 9, 10, 11]. In references [9, 10, 11] the emphasis is put on long-wavelength zonal flows. In references [7, 8], the derivation of the equations is valid for long and short-wavelengths but some approximations are used to describe the magnetic geometry.

### 3. Evaluation of the expressions for the residual zonal flow

The evaluation of the right side of equation (41) (and, of course, (44)) requires the calculation of quantities of the form

$$\{P\overline{Q}\}_s := \left\langle \sum_{\sigma=-1}^1 \int_0^{\infty} dv \int_0^{1/B} d\lambda \frac{\pi v^2 B}{\sqrt{1-\lambda B}} P\overline{Q} F_{s0} \right\rangle_{\psi}, \quad (46)$$

for functions  $P = P(\psi, \theta, \alpha, v, \lambda, \sigma)$  and  $Q = Q(\psi, \theta, \alpha, v, \lambda, \sigma)$ , where the orbit average is defined in (20). These averages depend on the details of the magnetic field and cannot be evaluated analytically, except in simplified cases (for example, in the cases considered

in [3, 5, 6]). In this work, we evaluate equation (41) using the framework of the code CAS3D-K [29, 30]. For this purpose, we have included in this code the relevant finite Larmor radius effects, the solution to the magnetic differential equations described in Appendix A, and the integration over the velocity coordinates  $v$  and  $\sigma$ .

The code CAS3D-K is well suited to perform the average (20). Since the lowest order particle trajectories lie entirely on flux surfaces, all the calculations are local, thus permitting a parallelization by flux surface using MPI. The magnetic equilibrium is obtained from the 3D MHD equilibrium code VMEC [31] and then transformed into Boozer coordinates  $\{\psi, \theta, \zeta\}$ , which can easily be transformed to the coordinates  $\{\psi, \theta, \alpha\}$ . On a given flux surface, the pitch angle  $\lambda$  distinguishes between passing and trapped trajectories. The passing-trapped boundary is given by  $\lambda_c = 1/B^{\max}$ , where  $B^{\max}$  is the maximum of  $B$  on the flux surface. Passing particles have  $\lambda$  values with  $0 < \lambda < \lambda_c$  and trapped particles are those with  $\lambda_c < \lambda < 1/B^{\min}$ , where  $B^{\min}$  is the minimum of  $B$  on the flux surface. Trapped particles can live inside one or several magnetic field periods. In CAS3D-K, they are grouped by the number of periods they go through. The groups are obtained by setting a large number of initial conditions for the trajectories, and finding the bounce points  $\theta_b$  from the bounce condition  $1 - \lambda B(\psi, \theta_b, \alpha) = 0$  for constant  $\psi$  and  $\alpha$ . From this procedure, the boundaries of each group are found and the numerical integration for a given group is performed by covering the region they define with new trajectories. Note that each group requires different numerical resolution. Some trapped trajectories close to the passing-trapped boundary may require a large number of periods until the bounce points are found. If this number is sufficiently large, typically larger than 500 periods, the trajectories are then considered as passing. A Gauss-Legendre quadrature scheme is used for the integration in  $\theta$ ,  $\alpha$  and  $\lambda$ , which avoids the numerical problems that may appear at points where  $1 - \lambda B = 0$ .

In reference [9], the phase space integrations with CAS3D-K discussed in the previous paragraph were employed to obtain the zonal flow frequency in stellarator geometry in the long-wavelength limit. In this limit, there are some simplifications. We have implemented new functionalities in CAS3D-K that also allow to deal with short wavelengths. Next, we describe the main features of this extension of CAS3D-K.

First, we note that the integration of the resulting expressions over the velocity coordinate  $v$  could be performed analytically in [9]. If one wants to calculate the averages involved in (41), the integration over the velocity coordinates  $v$  and  $\sigma$  must be computed numerically. We have included in CAS3D-K the integration over these coordinates on top of the  $\theta$ ,  $\alpha$  and  $\lambda$  integrations. For the integration over  $v$ , a linear scheme has been used. This scheme allows the computation of any moment in  $v$  of the Maxwellian distribution function,  $F_{s0}(\psi, v)$ .

Second, the equations to obtain the residual level (41) and (44) incorporate finite Larmor radius effects. These effects are encoded in  $J_0(k_{\perp}\rho_s)$ ,  $\Gamma_0(k_{\perp}^2\rho_{ts}^2)$  and  $\exp(\pm ik_{\psi}\delta_s)$ . Here,  $k_{\perp} = k_{\psi}|\nabla\psi|$  where  $k_{\psi}$  is an input parameter and the quantity  $|\nabla\psi| = |\nabla\psi|(\theta, \alpha)$  is obtained from the VMEC equilibrium. We have included those factors and adapted the

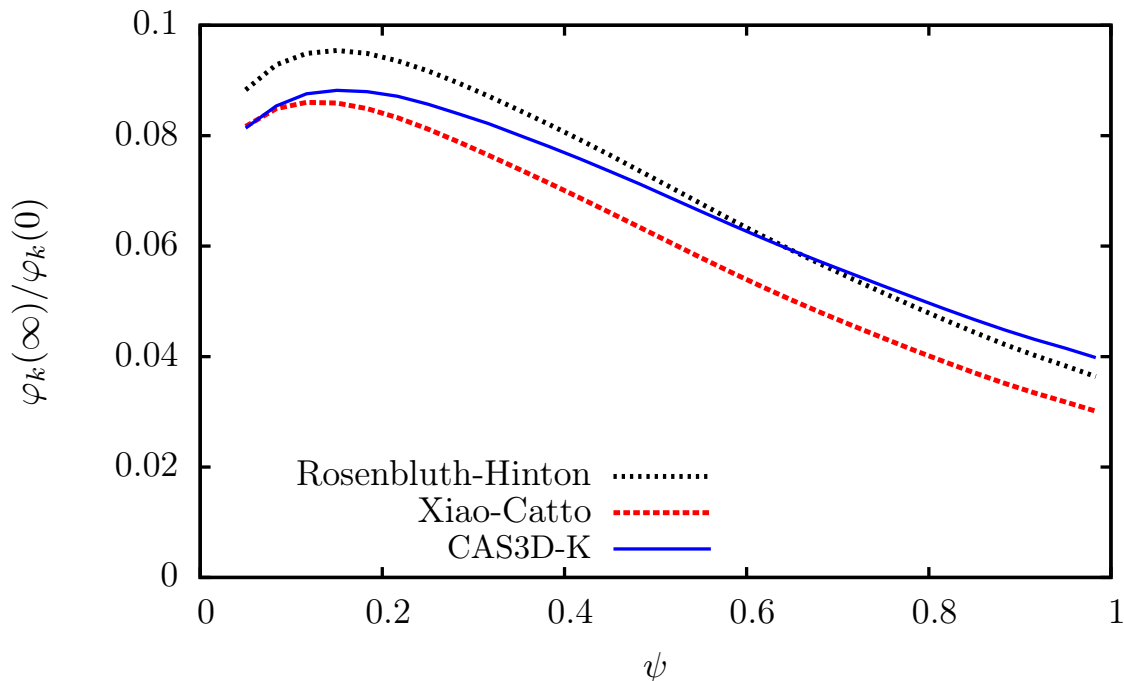


**Figure 1.** Radial dependence of the residual level given by (47), by (48), and by the evaluation of (44) with CAS3D-K in the long-wavelength limit. A tokamak with major radius  $R = 1.7$  m, minor radius  $a = 0.4$  m, and  $q$  profile given in figure 2 has been used.

resolution of the integration on phase space to their strong oscillatory behavior at short wavelengths. We have also implemented in the code the expression of  $\delta_s$  in stellarator geometry, for both passing and trapped particles (see the derivations in Appendix A). For passing particles,  $\delta_s$  is given by equation (A.7) and for trapped particles it is given by equation (A.17).

The above modifications included in CAS3D-K allow us to calculate the residual level in tokamak or stellarator geometry for arbitrary wavelengths. In the rest of the paper, we use the terminology “CAS3D-K” and “extension to CAS3D-K” interchangeably.

As a preliminary check of these extensions to CAS3D-K, in this section we compare our results with analytical results available in the literature. For these comparisons, we take a plasma consisting of singly charged ions and electrons, and assume flat density and temperature profiles with the same values for both species.

In reference [3], Rosenbluth and Hinton (R-H) calculated the residual level in large aspect ratio tokamaks with circular cross section and adiabatic electrons, in the limit  $k_\perp \rho_{ti} \ll 1$ . Denote the safety factor by  $q$  and the inverse aspect ratio by  $\varepsilon = (a/R)\sqrt{\psi}$ , where  $a$  is the minor radius and  $R$  is the major radius. The result obtained in [3] is

$$\frac{\varphi_k(\infty)}{\varphi_k(0)} = \frac{1}{1 + 1.6 q^2 \varepsilon^{-1/2}}. \quad (47)$$

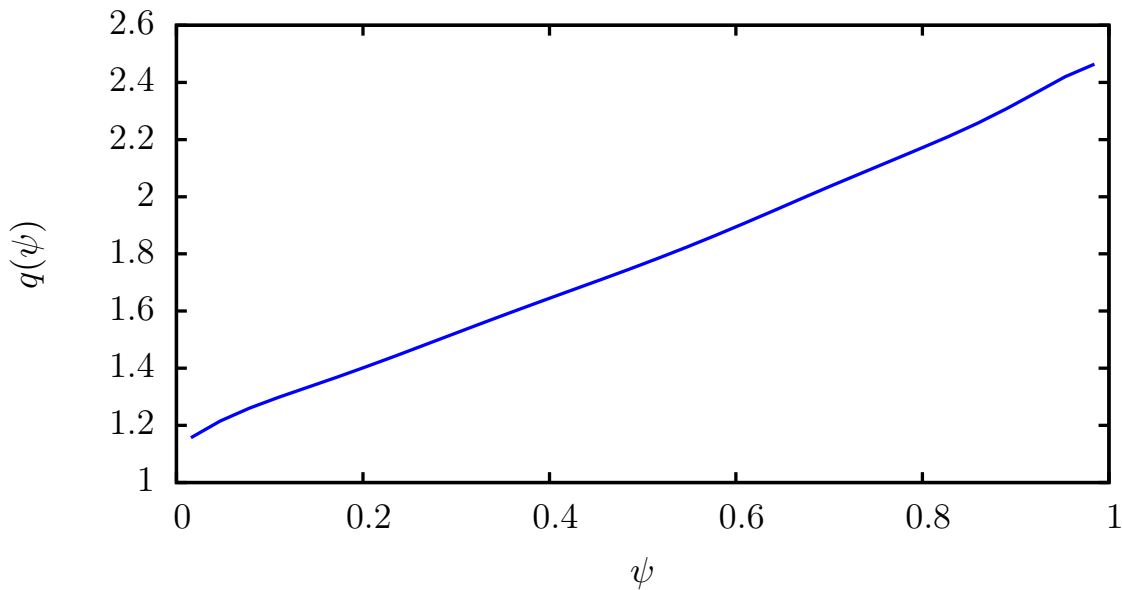


**Figure 2.** Safety factor profile of the tokamak employed for the calculations of Section 3.

In reference [5], Xiao and Catto gave an expression more accurate in the inverse aspect ratio expansion. Namely,

$$\frac{\varphi_k(\infty)}{\varphi_k(0)} = \frac{1}{1 + 1.6q^2\varepsilon^{-1/2} + 0.5q^2 + 0.36q^2\varepsilon^{1/2}}. \quad (48)$$

Both of these results were obtained by using the analytical equilibrium of a large aspect ratio circular tokamak which, in our coordinates, is given by

$$B = \frac{B_0}{1 + \varepsilon \cos(2\pi\theta)}, \quad (49)$$

where  $B_0$  is the magnetic field strength at the magnetic axis. The analytical solutions (47) and (48) are plotted in figure 1, together with the numerical evaluation of (44) with CAS3D-K, for  $k_{\perp}\rho_{ti} \ll 1$  and a Maxwellian initial condition. We use an axisymmetric tokamak with major radius  $R = 1.7$  m, minor radius  $a = 0.4$  m, and  $q$  profile given in figure 2. For the CAS3D-K computations, the equilibrium is obtained with VMEC employing the aspect ratio and safety factor values just mentioned. The wavenumber used in the CAS3D-K calculation is  $k_{\psi} = 0.5$  and the dimensionless quantity  $\langle k_{\perp}\rho_{ti} \rangle_{\psi}$  ranges from 0.0015 in the innermost radial position to 0.0068 in the outermost one. We have checked that the residual zonal flow value obtained with CAS3D-K and shown in figure 1 does not change if  $\langle k_{\perp}\rho_{ti} \rangle_{\psi}$  is further decreased. The regions of figure 1 where the curves agree and where the curves differ are as expected (see the remarks in [32] about figure 3(a) in that reference). The analytical equilibrium of a large aspect ratio circular tokamak, used in deriving the equations (47) and (48), differs less from the numerical equilibrium obtained with VMEC in radial positions closer to the center. We will see in Section 4 that the CAS3D-K results coincide with gyrokinetic simulations of zonal flow evolution, in which VMEC equilibria are also used.

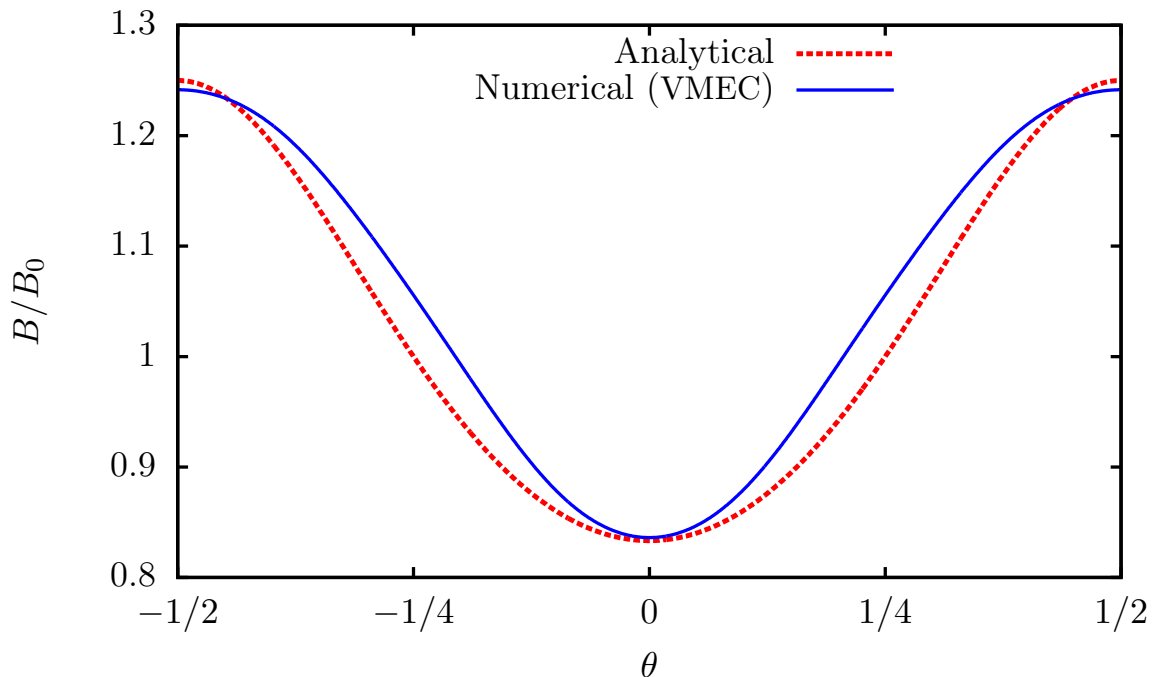


**Figure 3.** Magnetic field strength along a field line of the analytical large aspect ratio circular tokamak equilibrium, given by equation (49), with  $\varepsilon = 0.2$ , and for the numerical equilibrium obtained with VMEC (with  $R = 1.7$  m,  $a = 0.4$  m) at  $\psi = 0.7$ .

As explained above, Xiao and Catto (X-C) also addressed in references [5, 6] the extension of the calculation in [3] to short wavelengths. They gave the result

$$\frac{\varphi_k(\infty)}{\varphi_k(0)} = \frac{\sum_s \frac{Z_s^2}{T_s} \{1 - J_{0s}^2\}_s}{\sum_s \frac{Z_s^2}{T_s} \left\{1 - e^{-ik_\psi \delta_s} J_{0s} \overline{e^{ik_\psi \delta_s} J_{0s}}\right\}_s} \quad (50)$$

for the residual zonal flow in a tokamak at arbitrary wavelengths and with kinetic electrons. The expression provided by X-C for the case of adiabatic electrons is

$$\frac{\varphi_k(\infty)}{\varphi_k(0)} = \frac{\sum_{s \neq e} \frac{Z_s^2}{T_s} \{1 - J_{0s}^2\}_s}{\sum_{s \neq e} \frac{Z_s^2}{T_s} \left\{1 - e^{-ik_\psi \delta_s} J_{0s} \overline{e^{ik_\psi \delta_s} J_{0s}}\right\}_s}. \quad (51)$$

In order to avoid any confusion, we have to point out that (50) and (51) were not derived as the solution of the initial value problem explained in Section 2, but assuming that the quasineutrality equation is forced with a source term. The argument of X-C can be streamlined as follows. Go back to (41) for the tokamak case (that is,  $\overline{\omega_s} = 0$  for all particles). X-C consider that finite orbit width effects do not affect the initial condition; *i.e.*

$$\sum_s Z_s \left\{ e^{-ik_\psi \delta_s} J_{0s} \overline{e^{ik_\psi \delta_s} f_s(0)/F_{s0}} \right\}_s \approx \sum_s Z_s \left\{ J_{0s} f_s(0)/F_{s0} \right\}_s = \left\langle \sum_s Z_s \int J_{0s} f_s(0) d^3v \right\rangle_\psi. \quad (52)$$

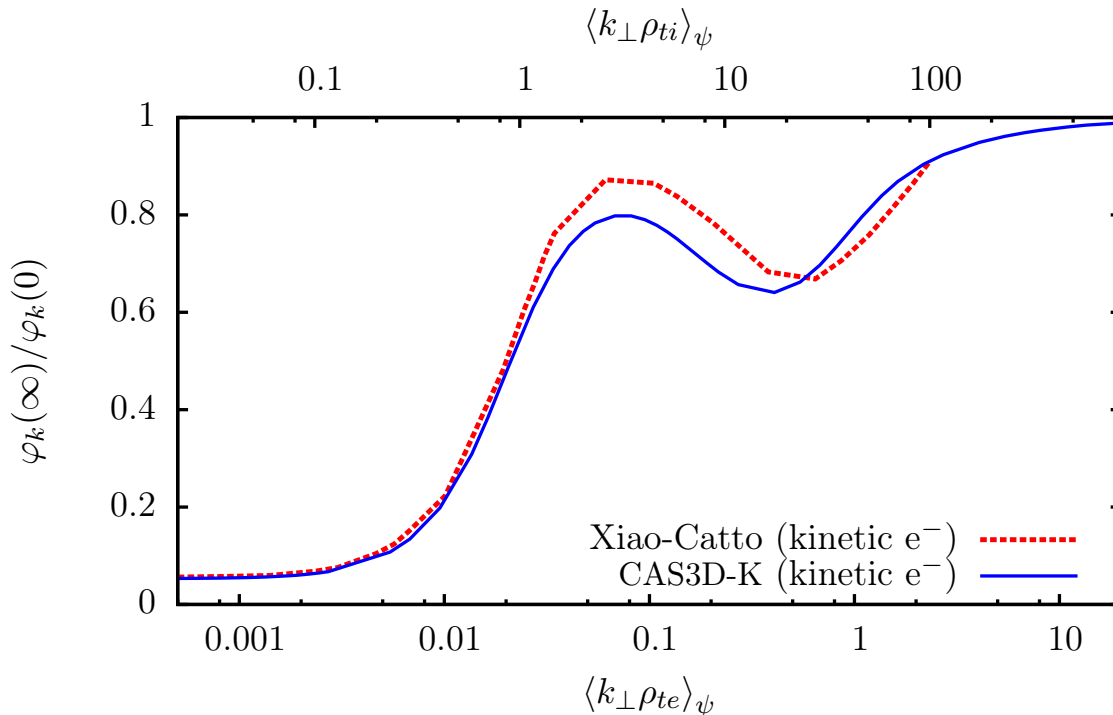


**Figure 4.** Comparison of the result in references [5, 6] and the evaluation of (50) with CAS3D-K. The parameters of the tokamak are the same as in figure 1.

Hence, in this approximation, (41) gives

$$\varphi_k(\infty) \approx \frac{\langle \sum_s Z_s \int J_{0s} f_s(0) d^3v \rangle_{\psi}}{\sum_s \frac{Z_s^2 e}{T_s} \left[ \{1\}_s - \left\{ e^{-ik_{\psi} \delta_s} J_{0s} \overline{e^{ik_{\psi} \delta_s} J_{0s}} \right\}_s^{\overline{\omega_s=0}} \right]}. \quad (53)$$

The quasineutrality equation at  $t = 0$ , (42), can be trivially rewritten as

$$\varphi_k(0) = \left( \sum_s \frac{Z_s^2 e}{T_s} \{1 - J_{0s}^2\}_s \right)^{-1} \left\langle \sum_s Z_s \int J_{0s} f_s(0) d^3v \right\rangle_{\psi}. \quad (54)$$

From the quotient of (53) and (54), one obtains equation (50). Analogously, one can obtain (51) from (44). From these manipulations, it is clear that in the X-C calculation the charge perturbation at  $t = 0$  can be viewed as a constant source term in the quasineutrality equation (see also the remark after equation (57)).

References [5] and [6] provided analytical evaluations of the right sides of (50) and (51) for simplified tokamak geometries. Since we can directly evaluate the right sides of (50) and (51) with CAS3D-K, we will compare the results as an additional check of our numerical tool.

In [5, 6], the analytical equilibrium of a circular cross section, large aspect ratio tokamak with safety factor  $q = 2$  and inverse aspect ratio  $\varepsilon = 0.2$  was used. For the calculations with CAS3D-K, we employ the VMEC tokamak equilibrium described above, which has similar parameters at  $\psi = 0.7$ . At this radial position, the VMEC equilibrium satisfies  $q = 2$  and  $\varepsilon = 0.2$  within an error of 1.5% ( $\varepsilon = 0.197$  and  $q = 2.03$ ). The

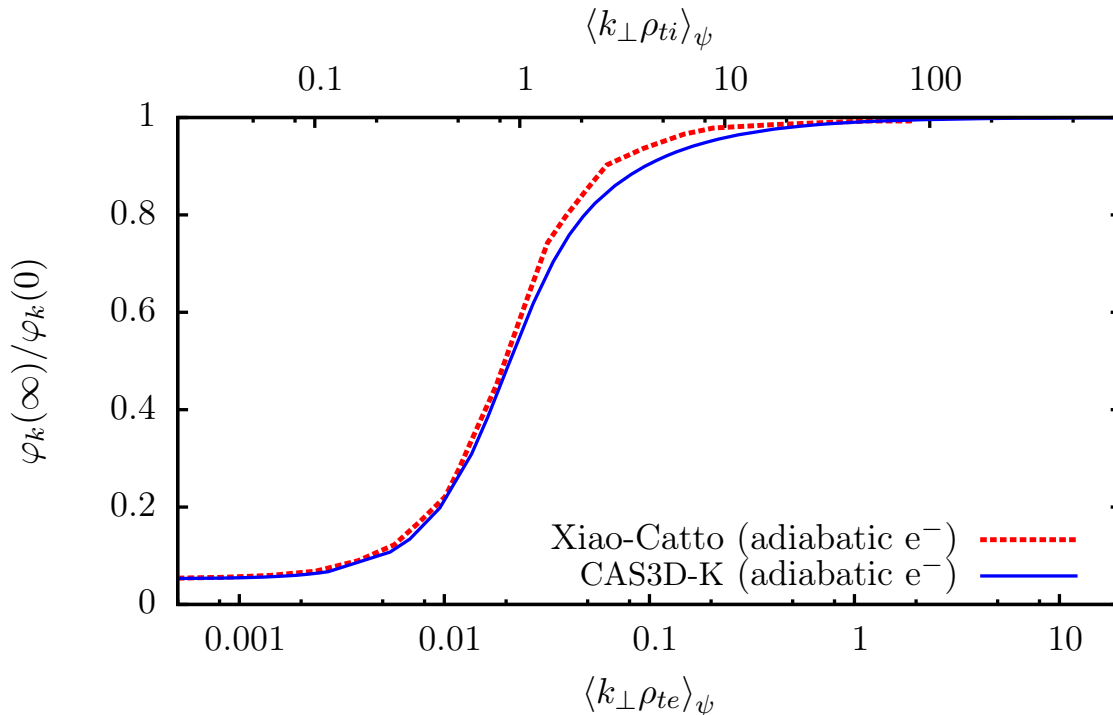


**Figure 5.** Comparison of the result in reference [5] for adiabatic electrons and the evaluation of equation (51) with CAS3D-K. The parameters of the tokamak are the same as in figure 1.

difference between the VMEC equilibrium and the analytical one is illustrated in figure 3, where we compare the magnetic field strength along a field line for both equilibria. In the VMEC equilibrium, the value of the magnetic field strength at the magnetic axis is  $B_0 = 1.87$  T. In general, deviations from circularity are expected in the numerical equilibrium because of effects like the Shafranov shift that are not taken into account in the analytical equilibrium. These deviations are smaller for radial positions closer to the center. The comparisons for the cases with fully kinetic species (50) and with adiabatic electrons (51) are shown in figures 4 and 5. The agreement is quite good. The fact that the curves present some differences, especially at short wavelengths, is not surprising because the equilibria are not identical. As already advanced above, we will see that the CAS3D-K calculations agree very well with the results from gyrokinetic simulations carried out with GENE coupled to GIST [15] and EUTERPE, that also employ VMEC equilibria. It should be noted that further gyrokinetic codes with similar capabilities exist. The independently developed code GKV-X [33], for instance, is also able to handle VMEC equilibria.

In the next section, we compare CAS3D-K calculations of the residual zonal flow with the results obtained from gyrokinetic simulations.

#### 4. Comparison of the residual zonal flow values obtained with CAS3D-K and with gyrokinetic simulations

In this section, we calculate the residual zonal flow as an initial value problem for a wide range of radial wavelengths in tokamak and stellarator geometries. We use the numerical techniques explained in Section 3 to evaluate the required averages using the code CAS3D-K. These calculations will be compared with the results from two gyrokinetic codes, showing that the extension of CAS3D-K is faster.

The residual level for the initial value problem is given by (41), once an initial condition  $f_s(0)$  has been specified. This initial condition has to satisfy (42). An initial condition fulfilling this equation is

$$f_s(0) = \frac{Z_s e \langle 1 - \Gamma_{0s} \rangle_\psi}{T_s \Gamma_{0s}} J_{0s} F_{s0} \varphi_k(0). \quad (55)$$

Using (55), we find that the expression for the residual level is

$$\frac{\varphi_k(\infty)}{\varphi_k(0)} = \frac{\sum_s \frac{Z_s^2}{T_s} \left\{ e^{-ik_\psi \delta_s} J_{0s} \overline{e^{ik_\psi \delta_s} J_{0s} \langle 1 - \Gamma_{0s} \rangle_\psi / \Gamma_{0s}} \right\}_s^{\overline{\omega_s=0}}}{\sum_s \frac{Z_s^2}{T_s} \left[ \{1\}_s - \left\{ e^{-ik_\psi \delta_s} J_{0s} \overline{e^{ik_\psi \delta_s} J_{0s}} \right\}_s^{\overline{\omega_s=0}} \right]}. \quad (56)$$

Similarly, from (44) and (55) we obtain the residual level when using the approximation of adiabatic electrons. Namely,

$$\frac{\varphi_k(\infty)}{\varphi_k(0)} = \frac{\sum_{s \neq e} \frac{Z_s^2}{T_s} \left\{ e^{-ik_\psi \delta_s} J_{0s} \overline{e^{ik_\psi \delta_s} J_{0s} \langle 1 - \Gamma_{0s} \rangle_\psi / \Gamma_{0s}} \right\}_s^{\overline{\omega_s=0}}}{\sum_{s \neq e} \frac{Z_s^2}{T_s} \left[ \{1\}_s - \left\{ e^{-ik_\psi \delta_s} J_{0s} \overline{e^{ik_\psi \delta_s} J_{0s}} \right\}_s^{\overline{\omega_s=0}} \right]}. \quad (57)$$

As explained above, in our numerical evaluations of (56) and (57) with CAS3D-K, we assume that in stellarator geometry the trapped trajectories have  $\overline{\omega_s} \neq 0$ .

To be precise, the Xiao and Catto formulas (50) and (51) can be obtained from an initial value problem calculation by choosing an initial condition  $f_s(0)$  different from ours. However, the initial conditions that recover the X-C results necessarily have increasingly fast oscillations along the orbit for increasing  $k_\psi$ , and seem of limited interest for the analysis of turbulence simulations. For this reason, we choose a different initial condition that is in our opinion more relevant.

The comparison with gyrokinetic simulations will be carried out by using the GENE and EUTERPE codes. GENE [12, 13, 14, 15] is a Eulerian gyrokinetic  $\delta f$  code which can be run in radially global, full flux surface or flux tube simulation domains. The code can use adiabatic or kinetic electrons and is able to deal with tokamak and stellarator geometries. In the GENE simulations, we calculate the zonal flow response for a wide range of radial wavelengths, using both adiabatic and kinetic electrons. EUTERPE [16, 17] is a global  $\delta f$  gyrokinetic code in 3D geometry with a Lagrangian Particle In Cell (PIC) scheme. In the simulations with EUTERPE, a  $k_\perp \rho_{ts} < 1$  approximation is employed in the quasineutrality equation that limits the range of wavelengths for which we can carry out the calculations. With EUTERPE,



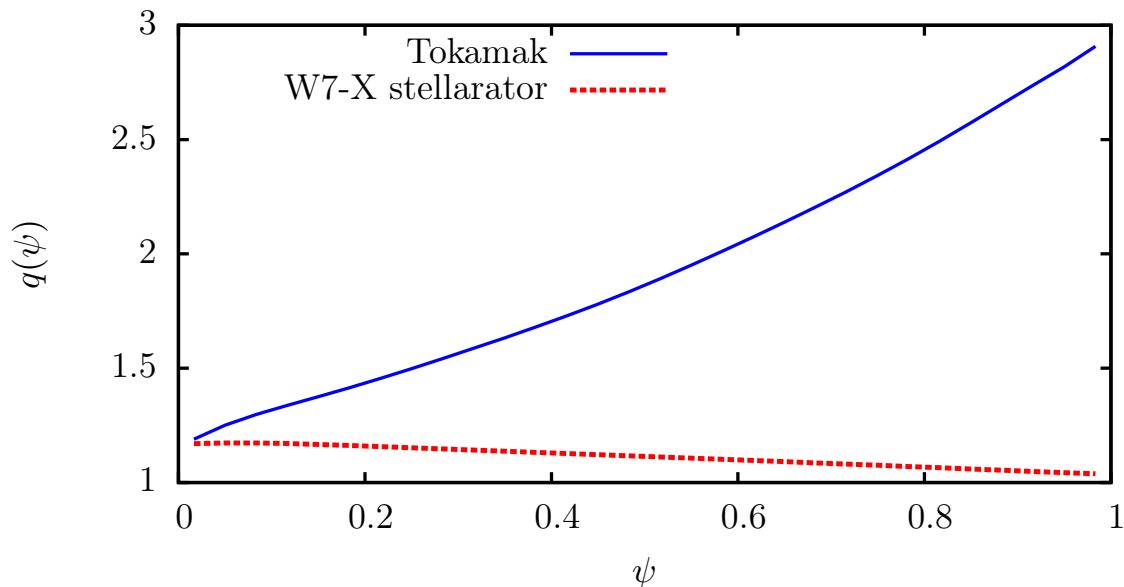


**Figure 6.** Safety factor profiles employed in Section 4 for the tokamak (solid line) and W7-X (dashed line) calculations.

we have been able to simulate adiabatic electrons and also kinetic heavy electrons. All the gyrokinetic simulations shown in this work are linear and collisionless, with a plasma that, unless stated otherwise, consists of only two species: singly charged ions and electrons,  $s = \{i, e\}$ . We take flat density and temperature profiles with the same values for both species.

In EUTERPE an initial condition proportional to  $\sin(k_\psi \psi)$  is used for the perturbed distribution function. After the first time step, a zonal perturbation to the potential with the same radial dependence  $\varphi(0) \propto \sin(k_\psi \psi)$  appears, that is used as the initial zonal flow. For the implementation of the initial condition in EUTERPE, the Bessel functions  $J_{0s}$  and  $\Gamma_{0s}$  are approximated to lowest order in  $k_\perp \rho_{ts} \ll 1$ . The initial condition in EUTERPE is then

$$F_{s1}(0) = \frac{Z_s e}{T_s} \langle k_\perp^2 \rho_{ts}^2 \rangle_\psi \varphi_k(0) \sin(k_\psi \psi) F_{s0}. \quad (58)$$

Since GENE works in Fourier space for the radial coordinate, we initialize the perturbed distribution function with only one radial mode which produces a potential with a single mode of unit amplitude.

#### 4.1. Tokamak

First, we compare gyrokinetic simulations and CAS3D-K calculations in tokamak geometry. We use an axisymmetric device with major radius  $R = 0.95$  m, minor radius  $a = 0.25$  m, and  $q$  profile given in figure 6, whose equilibrium is determined by VMEC. We use flat temperature profiles with  $T_i = T_e$ . The residual levels obtained with EUTERPE, CAS3D-K and the flux tube version of GENE are shown in figure 7 for

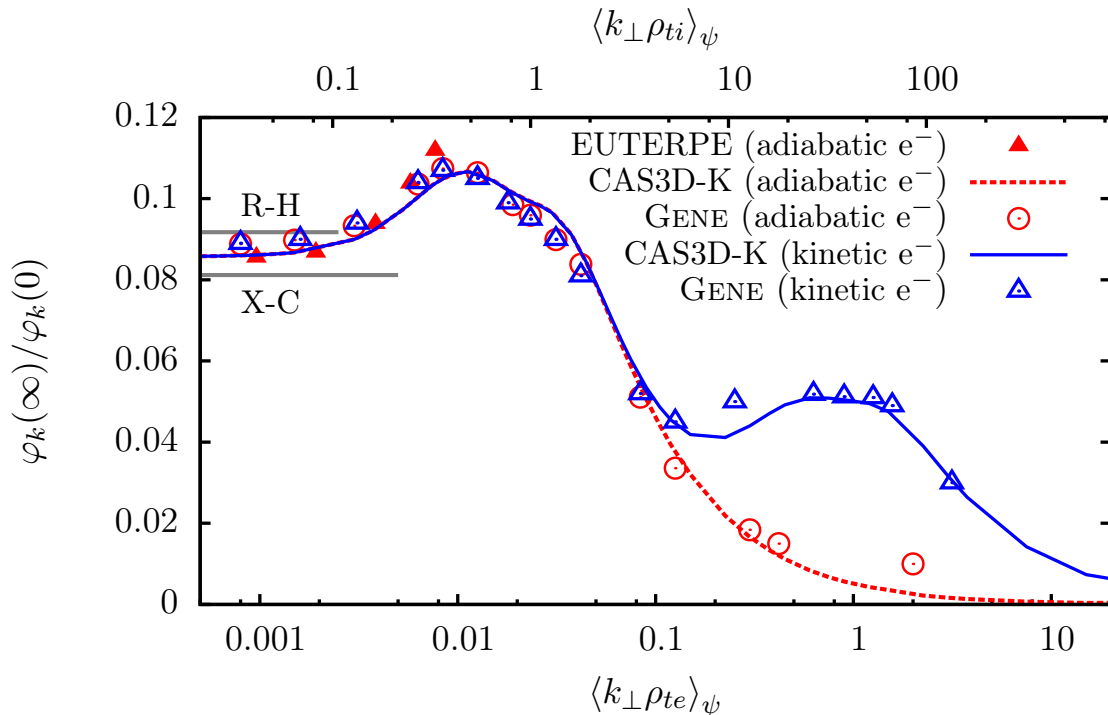


**Figure 7.** Residual zonal flow for the initial value problem in an axisymmetric large aspect ratio tokamak with major radius  $R = 0.95$  m, minor radius  $a = 0.25$  m and  $q$  profile given in figure 6. The values predicted by R-H and X-C (equations (47) and (48), respectively) are also shown for comparison.

a radial position  $\psi = 0.25$ . We show the calculations with fully kinetic species and also using the approximation of adiabatic electrons. The results of the gyrokinetic codes have been obtained fitting the temporal evolution of the potential to an exponential decay model

$$\varphi(t)/\varphi(0) = R + A \exp(-\xi t). \quad (59)$$

The results with CAS3D-K correspond to the evaluation of the equations (56) and (57). From figure 7, we can see that the agreement among the results of CAS3D-K, EUTERPE and GENE is excellent. When evaluating the residual level with gyrokinetic codes, a certain variability in the results must be assumed. This variability comes from the fitting method (smaller than 1%), the discretization in phase space and the control of the numerical noise, among other factors. All the results in this work obtained with GENE show variations smaller than 10%. In any case, figure 7 shows that the residual level obtained by the three independent methods coincides within a margin smaller than this quantity, which gives us confidence to consider that the overall error is quite small.

As can be seen in figure 7, the residual value has local maxima centered at the scales of the electron and ion Larmor radii. In the long-wavelength limit,  $k_{\perp} \rho_{ti} \ll 1$ , the residual level in a tokamak does not depend on  $k_{\perp}$ . Its value is well predicted by (47), and even more accurately by (48), for a large aspect ratio tokamak with circular cross section. For the VMEC equilibrium used here, these predictions (also indicated in figure

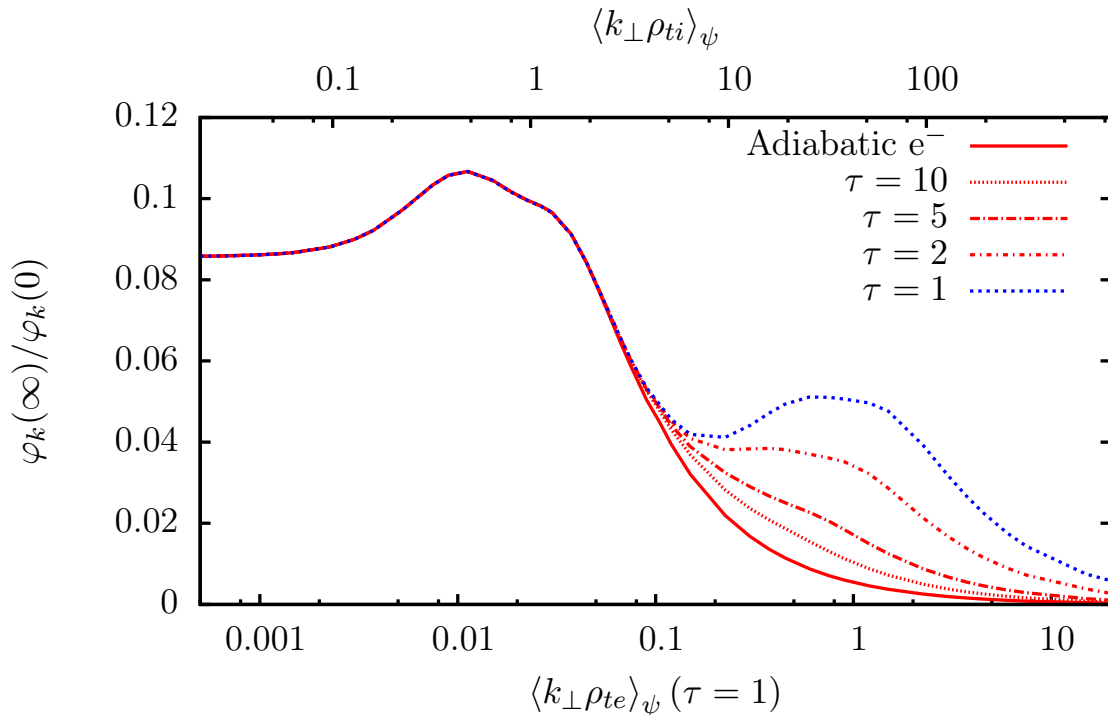


**Figure 8.** The same evaluation with CAS3D-K of equation (57) as in figure 7, with the adiabatic electron approximation, and the evaluation of equation (56) with fully kinetic species for different values of  $\tau$ .

7) are not so accurate for the reasons discussed in the paragraph below equation (48). At very short wavelengths,  $k_{\perp} \rho_{te} > 2$ , the residual value approaches zero as  $\langle k_{\perp} \rho_{ts} \rangle_{\psi}^{-1}$  when using fully kinetic species and also for the adiabatic electron approximation. In figure 7, it is shown that the adiabatic electron approximation in tokamaks is good for  $k_{\perp} \rho_{te} \lesssim 0.1$ . In figure 8, we reproduce the results with CAS3D-K in figure 7 together with the evaluation of (56) for different values of  $\tau := T_e/T_i$ . On the electron scale, the results with the adiabatic electron approximation and with kinetic electrons only coincide in the limit  $\tau \gg 1$ . Due to the reasons pointed out above, the simulations with EUTERPE have been carried out only for  $k_{\perp} \rho_{ti} < 1$ . Finally, it is obvious that the results of the forced system of figures 4 and 5 and the initial value problem of figure 7 behave in a completely different way for  $k_{\perp} \rho_{ti} \gtrsim 1$ .

#### 4.2. Stellarator

Now, we turn to stellarator geometry. We use an equilibrium for the standard configuration of the stellarator W7-X obtained with VMEC. The  $q$  profile is given in figure 6 and we take flat density and temperature profiles with  $T_i = T_e$ . In figure 9, calculations of the residual level with CAS3D-K, EUTERPE and the full flux surface version of GENE are shown for  $\psi = 0.25$ . Two curves correspond to CAS3D-K computations, one using adiabatic electrons (see equation (57)) and the other one using kinetic electrons (see equation (56)). In figure 9, the results of the gyrokinetic

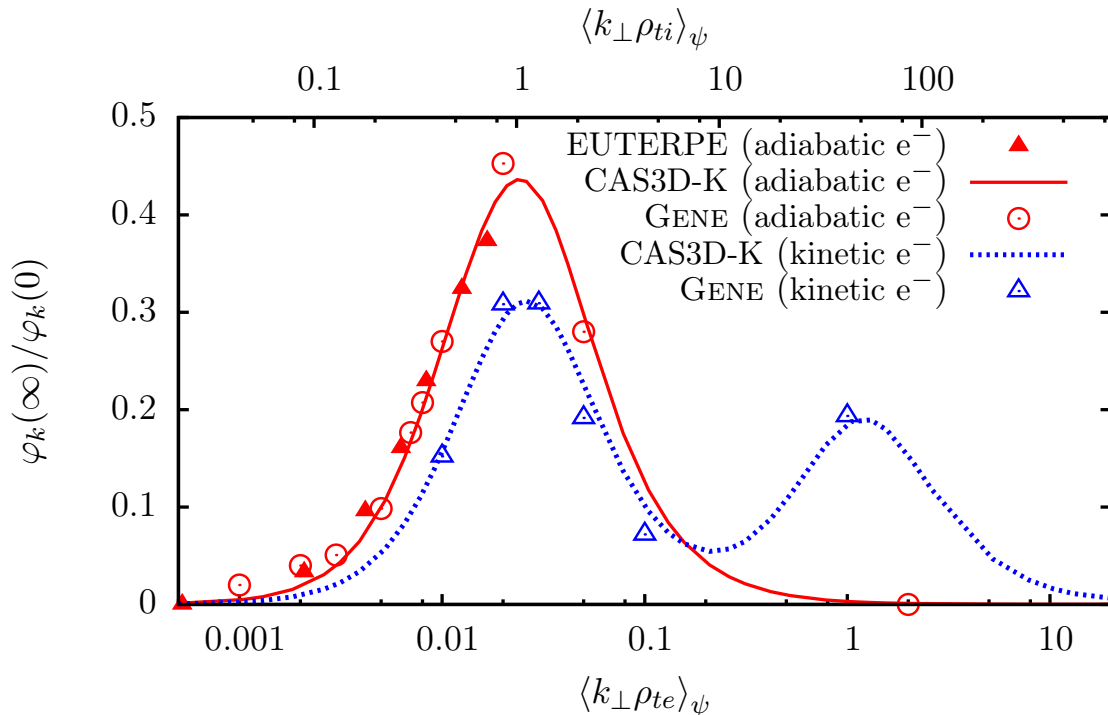


**Figure 9.** Residual zonal flow level for the initial value problem in the standard configuration of the W7-X stellarator at  $\psi = 0.25$ . The  $q$  profile is shown in figure 6.

simulations were obtained employing both the approximation of adiabatic electrons and fully kinetic species with GENE, whereas only calculations with adiabatic electrons are shown for EUTERPE. These results have been fitted to an exponential decay model (59) to get the residual value. Similar results can be obtained with an algebraic decay model as suggested in reference [10]. The results of CAS3D-K show remarkable agreement with both gyrokinetic codes.

As explained and quantified at the end of this section, the gyrokinetic simulations with kinetic species are much more demanding in terms of computational resources than those with adiabatic electrons. Global simulations with EUTERPE using fully kinetic electrons in stellarator geometry would require an extremely large computing time. This time can be reduced by increasing the mass of the species involved. We have calculated for deuterium ions and kinetic heavy electrons  $s = \{D, E\}$ , with  $m_E = 400 m_e$  and  $T_D = T_E$ . The results are shown in figure 10 where we compare the residual level calculated with EUTERPE and CAS3D-K at  $\psi = 0.25$ . The results with adiabatic electrons shown in this figure are exactly the same as those with adiabatic electrons in figure 9, obtained for hydrogen ions. Note that, with adiabatic electrons, as the residual level only depends on  $\langle k_{\perp} \rho_{ti} \rangle_{\psi}$ , the curves for hydrogen or deuterium ions are exactly the same.

In figure 9, like in tokamaks, we find local maxima of the residual level centered around the scales of the electron and ion Larmor radii. However, at long wavelengths,  $k_{\perp} \rho_{ti} \ll 1$ , the residual level as a function of  $k_{\perp} \rho_{ti}$  behaves very differently in tokamaks and in stellarators (see, for example, figures 7 and 9). This can be easily understood

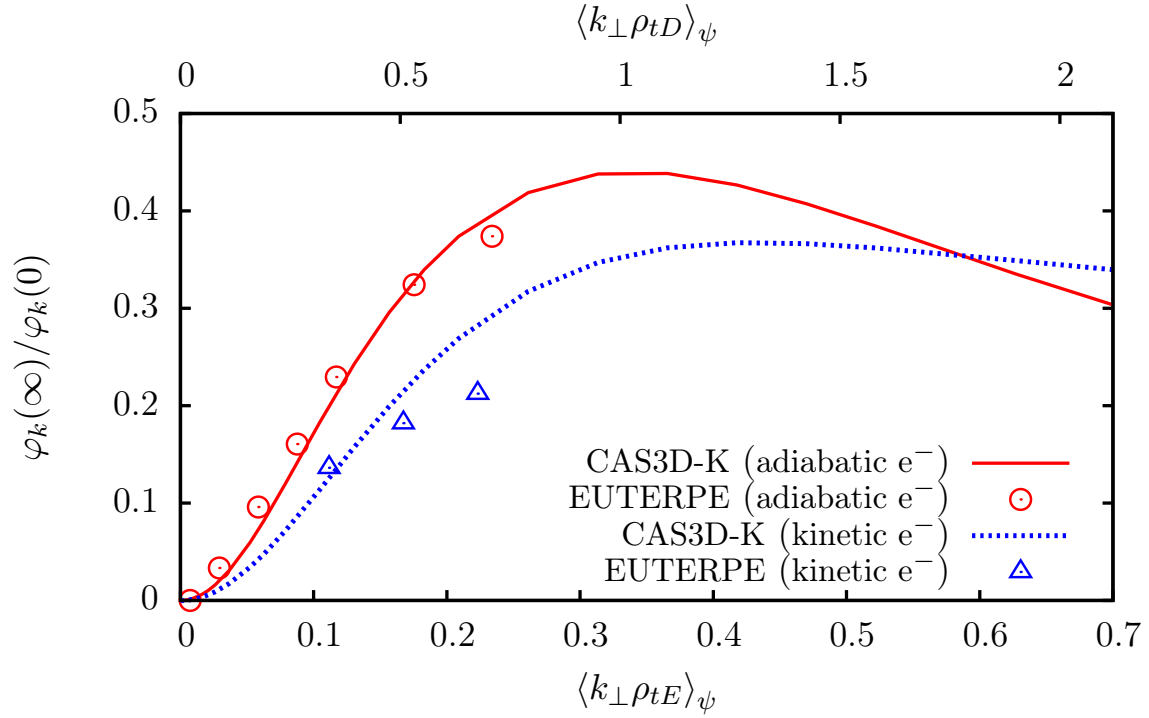


**Figure 10.** Residual zonal flow level for the initial value problem in the standard configuration of the W7-X stellarator at  $\psi = 0.25$ , with deuterium ions ( $D$ ) and kinetic heavy electrons ( $E$ ) ( $m_E = 400m_e$ ) and also using the approximation of adiabatic electrons.

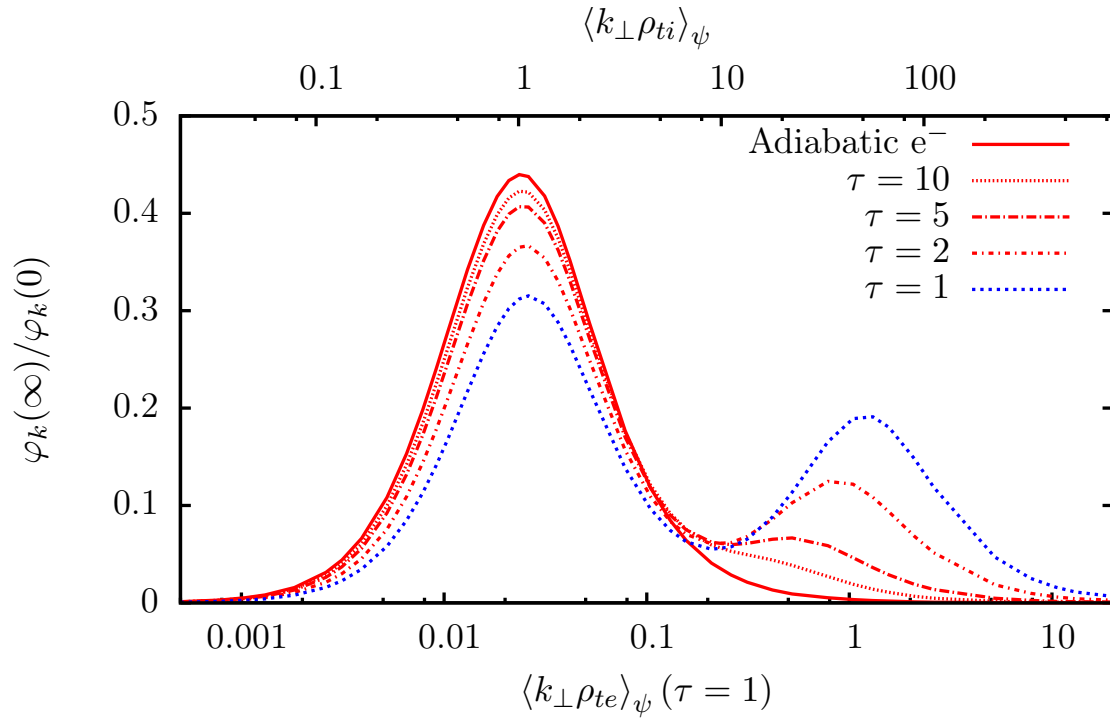


**Figure 11.** The same evaluation with CAS3D-K of equation (57) as in figure 9, with the adiabatic electron approximation, and the evaluation of equation (56) with fully kinetic species for different values of  $\tau$ .

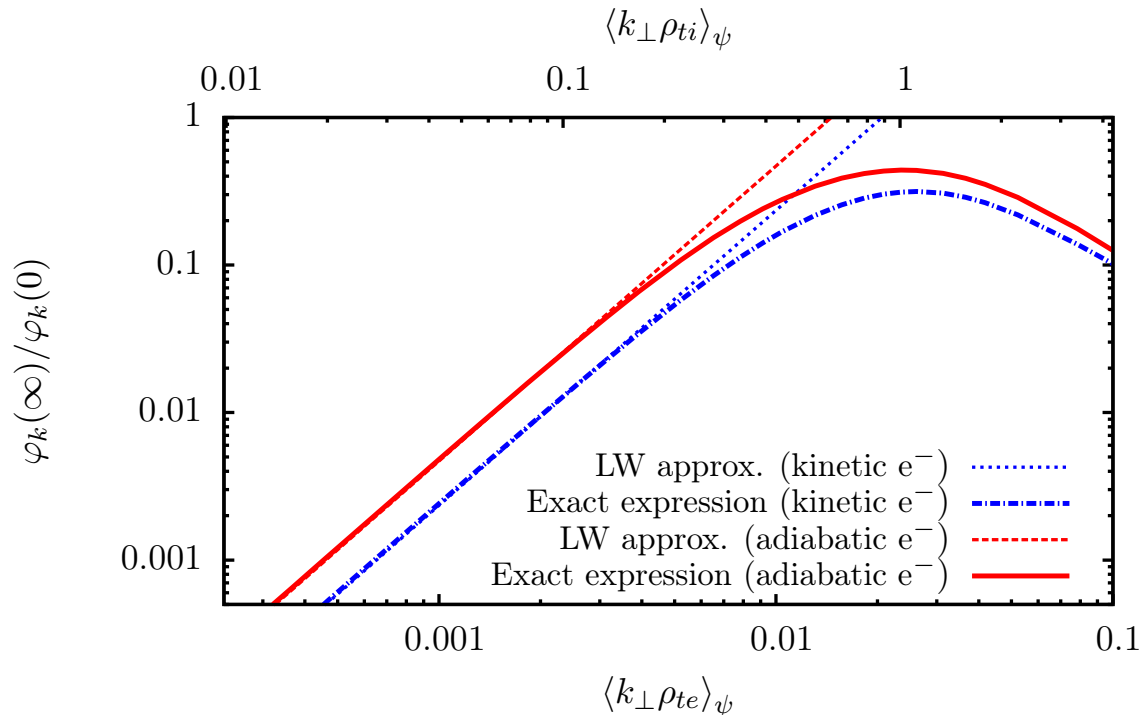


**Figure 12.** Range of validity of the long-wavelength (LW) approximations, when using fully kinetic species (60) and with the approximation of adiabatic electrons (61), compared to the exact expressions (56) and (57), in the standard configuration of the W7-X stellarator at  $\psi = 0.25$  and with  $T_i = T_e$ .

by expanding (56) and (57) in  $k_{\perp} \rho_{ti} \ll 1$ . The numerator of these expressions scales quadratically with  $k_{\perp} \rho_{ti}$  in tokamaks and stellarators. The difference comes from the denominator. In a stellarator, the denominator is non-zero when  $k_{\perp} \rho_{ti} = 0$ . However, in a tokamak the denominator scales quadratically with  $k_{\perp} \rho_{ti}$ . The denominator has been often related to the shielding effects of collisionless classical and neoclassical polarization currents [3, 4, 5, 6].

It is worth giving explicitly the  $k_{\perp} \rho_{ti} \ll 1$  expansions of (56) and (57) in a stellarator and discussing a stellarator specific point in detail. The lowest order term of (56) gives

$$\frac{\varphi_k(\infty)}{\varphi_k(0)} = \frac{(1 - \epsilon_t) \langle k_{\perp} \rho_{ti} \rangle_{\psi}^2}{\epsilon_t (1 + T_i / (Z_i^2 T_e))} + O(\langle k_{\perp} \rho_{ti} \rangle_{\psi}^4), \quad (60)$$

where  $\epsilon_t = n_s^{-1} \{1\}_s^{\text{trapped}}$  is the fraction of trapped particles. Here, the superindex “trapped” means that the phase space integration is performed only over the trapped region. However, if we use the approximation of adiabatic electrons, (57), we find

$$\frac{\varphi_k(\infty)}{\varphi_k(0)} = \frac{(1 - \epsilon_t) \langle k_{\perp} \rho_{ti} \rangle_{\psi}^2}{\epsilon_t} + O(\langle k_{\perp} \rho_{ti} \rangle_{\psi}^4). \quad (61)$$

Hence, in stellarators, the adiabatic electron approximation gives an incorrect residual zonal flow, even at long wavelengths. This has been pointed out in references [7, 8] and is confirmed by the calculations shown in figures 9 and 10. The curves in figure 11 for different values of  $\tau$  quantify the error of the adiabatic electron approximation

for any wavelength. As can be seen in this figure, the residual level obtained with this approximation, only coincides with that obtained with fully kinetic species in the limit  $\tau \gg 1$ . In figure 12, we plot the curves in figure 9 corresponding to CAS3D-K together with the evaluation of their expansions to lowest order in  $k_{\perp}\rho_{ti} \ll 1$ , (60) and (61). It is clear from figure 12 that (60) and (61) are good approximations of (56) and (57) respectively for  $k_{\perp}\rho_{ti} \lesssim 0.2$ .

We point out that at scales comparable to the ion Larmor radius,  $k_{\perp}\rho_{ti} \sim 1$ , the residual level appears to be larger in stellarators than in tokamaks (see, for example, figures 8 and 11). In order to discard trivial explanations, we have studied with CAS3D-K the residual level in a tokamak configuration with the same aspect ratio and  $q$  profile as those of the standard configuration of W7-X and the results are much closer to the tokamak case than to the stellarator results. This is not surprising because, as shown in reference [6], not only the aspect ratio but also shaping effects like elongation, triangularity and Shafranov shift, among others, affect the residual level. We leave for a future work a detailed study of the magnetic configuration influence on the residual level.

#### 4.3. Simulation conditions and computational time

The converged results shown in this work require disparate computing resources, depending on the code and the physical problem. The relevant numerical parameters and the computational resources required by each code are described below.

In CAS3D-K, we used 256 points for the integration over the velocity coordinate  $v$ , with  $0 \leq v \leq 4\pi v_{ts}$ . For the integration over the  $\lambda$  coordinate, we used 72 integration points in the tokamak and 24 in W7-X. Along the field line, we used 32 points at long wavelengths and up to 4096 for short wavelengths. This resolution allows the correct integration of the highly oscillatory functions. Thanks to axisymmetry, in a tokamak all field lines on a flux surface are equivalent. In W7-X, we used 1024 field lines to cover the flux surface for passing particles. For the evaluation of  $\delta_s$  in the stellarator case, all the modes with  $|m| \leq 8$  and  $|n| \leq 8$  were retained. The calculations were carried out in the EULER cluster at CIEMAT, equipped with Xeon 5450 quadcore processors at 3 GHz and 4XDDR Infiniband network.

In GENE, a 1D spatial grid along the field line ( $z$  coordinate) is used in the tokamak cases while in stellarator simulations a 2D spatial grid in coordinates  $(y, z)$  is used to describe a full flux surface ( $y$  is the coordinate along the binormal direction). In velocity space, a 2D grid in parallel velocity and magnetic moment coordinates  $(v_{\parallel}, \mu)$  is used in both the tokamak and the stellarator cases. The resolution of the spatial and velocity grids used are given in table 1 together with the time step and the total simulation time for each case. Times are given in  $1/\Omega_G$  units, with  $\Omega_G = a/v_{te}$ , where we recall that  $a$  is the minor radius and  $v_{te}$  is the thermal velocity of electrons. The GENE simulations were run in HYDRA [34], equipped with Intel Ivybridge at 2.8 GHz and SandyBridge-EP at 2.6 GHz processors interconnected by Infiniband FDR14.

**Table 1.** Numerical parameters used in GENE simulations. The time step ( $\Delta t_G$ ) and the total simulation time ( $T_G$ ) are given in  $\Omega_G^{-1}$  units, with  $\Omega_G = a/v_{te}$ .

|                   | long wavelength ( $k_\perp \rho_{ti} < 1$ ) |                        | short wavelength ( $k_\perp \rho_{ti} > 1$ ) |                        |             |
|-------------------|---|------------------------|--|------------------------|-------------|
|                   | adiabatic e <sup>-</sup>                    | kinetic e <sup>-</sup> | adiabatic e <sup>-</sup>                     | kinetic e <sup>-</sup> |             |
| $n_z$             | 64  | 64                     | 128  | 256                    |             |
| $n_{v_\parallel}$ | 128   | 1024                   | 1024 – 2048                                  | 2048 – 4096            |             |
| $n_\mu$           | 40  | 40                     | 40   | 40                     | tokamak     |
| $\Delta t_G$      | 1 – 6                                       | 0.03 – 0.06            | 0.2 – 1                                      | 0.02                   |             |
| $T_G$             | 4000 – 15000                                | 3000 – 10000           | 4000 – 10000                                 | 150                    |             |
| $n_y$             | 64  | 64                     | 64   | 64                     |             |
| $n_z$             | 256   | 128                    | 128  | 128                    |             |
| $n_{v_\parallel}$ | 128   | 256 – 512              | 128  | 128 – 512              | stellarator |
| $n_\mu$           | 20  | 20                     | 20   | 10 – 20                |             |
| $\Delta t_G$      | 4 – 8                                       | 0.06                   | 0.2 – 5                                      | 0.06                   |             |
| $T_G$             | 100000 – 200000                             | 40000                  | 300 – 5000                                   | 10000 – 550000         |             |

**Table 2.** Numerical parameters used in EUTERPE simulations. The time step ( $\Delta t_E$ ) and the total simulation time ( $T_E$ ) are given in  $\Omega_E^{-1}$  units, with  $\Omega_E = eB^*/m$ . <sup>†</sup>This range corresponds to calculations with deuterium ions and heavy electrons. <sup>††</sup>Only for the shortest-wavelength case.

| long wavelength<br>( $k_\perp \rho_{ti} < 1$ ) | tokamak                  |                        | stellarator              |                         |
|--|--------------------------|------------------------|--------------------------|-------------------------|
|  | adiabatic e <sup>-</sup> | kinetic e <sup>-</sup> | adiabatic e <sup>-</sup> | kinetic e <sup>-†</sup> |
| $n_{s_E}$                                      | 32 – 192                 | —                      | 64 – 192                 | 32 – 96                 |
| $n_{\theta_E} \times n_{\phi_E}$               | 16 × 16                  | —                      | 32 × 32                  | 16 × 16                 |
| # of markers                                   | 40 M – 240 M             | —                      | 40 M – 240 M             | 40 M – 120 M            |
| filter cutoff                                  | 5                        | —                      | 5, 10 <sup>††</sup>      | 5                       |
| $\Delta t_E$                                   | 10 – 5                   | —                      | 50 – 20                  | 0.5                     |
| $T_E$  | 60000                    | —                      | 400000                   | 45000                   |

In EUTERPE, the electric potential is represented in a 3D spatial grid in PEST coordinates ( $s_E, \theta_E, \phi_E$ ) whose radial resolution must be large enough to correctly represent the potential perturbation. The number of markers was set according to the grid resolution to maintain the ratio of markers per grid cell approximately constant. A low-pass squared filter in Fourier space ( $k_{\theta_E}, k_{\phi_E}$ ) is used to reduce the noise. In table 2 the resolution of the spatial grid ( $n_{s_E}, n_{\theta_E}, n_{\phi_E}$ ), the number of markers, the filter cutoff, the time step and the total simulation time used for each case are given. Times are given in  $1/\Omega_E$  units, where  $\Omega_E = eB^*/m_i$ ,  $e$  is the elementary charge,  $m_i$  is the ion mass and  $B^*$  is the average of the magnetic field along the magnetic axis. The EUTERPE simulations were carried out in EULER and MareNostrum III [35], equipped with Intel SandyBridge-EP processors at 2.6 GHz and Infiniband FDR10 interconnection.

In table 3 we illustrate the computational cost, in total CPU core hours (that is,



**Table 3.** Estimated CPU time (total core hours) to obtain the residual zonal flow value with the different codes. We give estimations for tokamaks and stellarators; for adiabatic and kinetic electrons; and for long and short wavelengths. <sup>†</sup>This range corresponds to calculations with deuterium ions and heavy electrons. <sup>††</sup>For very small wavenumbers, GENE computes the residual zonal flow in a tokamak in approximately 0.5 CPU hours.

|         | long wavelength ( $k_{\perp}\rho_{ti} < 1$ ) |                        | short wavelength ( $k_{\perp}\rho_{ti} > 1$ ) |                        |             |
|---------|--|------------------------|---|------------------------|-------------|
|         | adiabatic e <sup>-</sup>                     | kinetic e <sup>-</sup> | adiabatic e <sup>-</sup>                      | kinetic e <sup>-</sup> |             |
| CAS3D-K | 1.5  | 3                      | 15  | 30                     |             |
| GENE    | 10 <sup>††</sup>                             | 1300                   | 150   | 200                    | tokamak     |
| EUTERPE | 7000   | —                      | —   | —                      |             |
| CAS3D-K | 0.5  | 1                      | 4   | 8                      |             |
| GENE    | 2000   | 40000                  | 200   | 250000                 | stellarator |
| EUTERPE | 20000  | 80000 <sup>†</sup>     | —   | —                      |             |

the time summed up over all the cores employed in the simulation), for the different codes and cases studied. Of course, the values shown in table 3 are simply indicative, as they depend on the numerical details of the simulations and the type of CPU employed in each calculation. In addition, a systematic analysis of the optimal resolution to carry out the computations with each code has not been performed. The main conclusion that we can extract from table 3 is that determining the residual zonal flow with CAS3D-K is faster than with GENE and EUTERPE. This is specially true for stellarators. The reason is that in stellarators only passing particles contribute to the residual value, while in tokamaks also trapped particles count, and trapped trajectories typically demand a more careful numerical treatment than passing ones. Whereas the CAS3D-K calculation simply drops the contribution from the trapped region, the gyrokinetic runs simulate all trajectories. However, we can see from table 3 that the computational cost when using the gyrokinetic codes is higher in stellarator geometry because it requires increased resolution in phase space to obtain converged results.

We observe that EUTERPE, a 3D global code, requires much more CPU time than GENE, particularly in the tokamak case, in which the flux tube version of GENE is used. The reason is that EUTERPE simulates the whole plasma while GENE is here operated in a radially local limit. The computational cost with EUTERPE increases with  $k_{\perp}\rho_{ti}$ , because more flux surfaces have to be considered as  $k_{\perp}$  increases to properly resolve the radial structure of the potential in all the plasma volume. In EUTERPE the different values of  $k_{\perp}\rho_{ti}$  at a given radial position are obtained by keeping the value of  $\rho_{ti}$  (determined by the ion mass, the temperature and the magnetic field) and varying the value of  $k_{\perp}$ . In CAS3D-K, the resolution at short wavelengths must be increased to correctly calculate the highly oscillatory functions related to the finite orbit width and the finite Larmor radius effects.

The analytical expression obtained by Rosenbluth and Hinton in reference [3], given by equation (47), has been largely used as a linear benchmark for gyrokinetic codes in

tokamak geometry and in the long-wavelength limit. The results presented in this work show that CAS3D-K can be used to perform those benchmarks not only in tokamak geometry but also in stellarator geometry and for arbitrary wavelengths. Examples of such benchmarks are given in figure 7 for the global code EUTERPE and the flux tube version of GENE in tokamak geometry, and in figure 9 for EUTERPE and the full flux surface version of GENE in stellarator geometry.

Finally, it is a matter of fact that the tokamak calculation including a source term in the quasineutrality equation [5, 6] has become quite popular in the literature. Just for completeness, we give an analogous calculation for the stellarator in Appendix B using gyrokinetic simulations and CAS3D-K. We also show the results for the tokamak using gyrokinetic codes (these were not included in Section 3).

## 5. Conclusions

In this work we have treated analytically the linear collisionless zonal flow evolution as an initial value problem, and derived expressions (see (41) and (44)) for the residual value that are valid for arbitrary wavelengths and for tokamak and stellarator geometries. The expressions (41) and (44) involve certain averages in phase space, and also the solution of magnetic differential equations, that cannot be evaluated analytically except for very special situations. We have extended the code CAS3D-K to evaluate such expressions in general. We have tested the extension of the code by comparing its results with analytical formulae available in the literature for simplified tokamak geometry [5, 6]. These tests are given in figures 1, 4 and 5.

Then, we have computed the residual zonal flow level in tokamak and stellarator geometries for a wide range of radial wavelengths, using both the approximation of adiabatic electrons and fully kinetic electrons. We have compared the results of CAS3D-K with those obtained from two gyrokinetic codes: the global code EUTERPE and the radially local versions of GENE (full flux surface and flux tube). The comparisons are shown in figures 7, 9 and 10.

A stellarator specific effect has been discussed in detail. Namely, the fact that the adiabatic electron approximation gives incorrect zonal flow residuals even for  $k_{\perp}\rho_{ti} \ll 1$ , unlike in tokamaks. This effect has also been confirmed by means of gyrokinetic simulations. This is shown in figures 9, 10 and 11.

Finally, we stress the efficiency of our method to determine the residual zonal flow. Gyrokinetic simulations with GENE and EUTERPE to obtain the residual level are computationally expensive, especially with fully kinetic species, in the short-wavelength region, and in stellarator geometry. On the contrary, the calculations with CAS3D-K are less demanding (see table 3), particularly in stellarator geometry. These results show that CAS3D-K is a useful tool to calculate fast and accurately the residual level in any toroidal geometry and for arbitrary wavelengths. This code is even more useful in stellarator geometry as kinetic electrons must be considered to correctly calculate the residual level. It can also provide a good benchmark for gyrokinetic codes.

## Acknowledgments

The authors thank Peter Catto, Bill Dorland, Per Helander, Alexey Mishchenko and Yong Xiao for helpful discussions, and Antonio López-Fraguas for his help with the usage of VMEC. The authors thankfully acknowledge the computer resources, technical expertise and assistance provided by the Barcelona Supercomputing Center (BSC), the Rechenzentrum Garching (RZG) and the Computing Center of CIEMAT.

This research has been funded in part by grant ENE2012-30832, Ministerio de Economía y Competitividad (Spain) and by an FPI-CIEMAT PhD fellowship. This work has been carried out within the framework of the EUROfusion Consortium and has received funding from the Euratom research and training programme 2014-2018 under grant agreement No 633053. The views and opinions expressed herein do not necessarily reflect those of the European Commission.

## Appendix A. Magnetic differential equation

In this section, we give the solution  $\delta_s$  to the magnetic differential equation (23). We use Boozer coordinates. That is, we assume that  $\{\psi, \theta, \zeta\}$  are such that the contravariant form of  $\mathbf{B}$  is given by (5), and its covariant form is given by

$$\mathbf{B} = I_t \nabla \theta - I_p \nabla \zeta + \tilde{\beta}(\psi, \theta, \zeta) \nabla \psi. \quad (\text{A.1})$$

The square root of the metric determinant is  $\sqrt{g} = (I_t \Psi'_p - I_p \Psi'_t) / B^2$ . Here,  $I_t = I_t(\psi)$  and  $I_p = I_p(\psi)$  are the toroidal and poloidal currents, respectively. In Boozer coordinates, the radial magnetic drift reads

$$\omega_s = -\frac{1}{\tau_b \Psi'_p} [I_p \partial_\theta + I_t \partial_\zeta] \rho_{\parallel s}. \quad (\text{A.2})$$

The parallel gyroradius is defined as  $\rho_{\parallel s} = v_{\parallel} / \Omega_s$ , whereas  $\tau_b = B \sqrt{g} / (v_{\parallel} \Psi'_p)$ .

### Appendix A.1. Magnetic differential equation for passing particles

For passing particles,  $\overline{\omega_s} = 0$ . The magnetic differential equation to be solved is then given by

$$v_{\parallel} \hat{\mathbf{b}} \cdot \nabla \delta_s = \omega_s, \quad (\text{A.3})$$

which in Boozer coordinates becomes

$$(\Psi'_p \partial_\theta + \Psi'_t \partial_\zeta) \delta_s = - (I_p \partial_\theta + I_t \partial_\zeta) \rho_{\parallel s}. \quad (\text{A.4})$$

This equation is easily solved in Fourier space, giving

$$\delta_s = C - \sum_{m,n \neq 0} \left[ \frac{m I_p + n I_t}{m \Psi'_p + n \Psi'_t} \right] (\rho_{\parallel s})_{mn} e^{2\pi i(m\theta + n\zeta)}, \quad (\text{A.5})$$

where the coefficients  $(\rho_{\parallel s})_{mn}$  are defined by

$$\rho_{\parallel s} = \sum_{m,n} (\rho_{\parallel s})_{mn} e^{2\pi i(m\theta + n\zeta)} \quad (\text{A.6})$$

and  $C$  is a constant. By choosing the integration constant as  $C = -I_p(\rho_{\parallel s})_{00}/\Psi'_p$ , we have

$$\delta_s = -\frac{I_p}{\Psi'_p} \left[ \rho_{\parallel s} + \left( \frac{I_t}{qI_p} - 1 \right) \sum_{m,n \neq 0} \left( \frac{qn}{m+qn} \right) (\rho_{\parallel s})_{mn} e^{2\pi i(m\theta+n\zeta)} \right]. \quad (\text{A.7})$$

This solution, already given in [9], is valid for any toroidal geometry. For axisymmetric tokamaks, it reduces to  $\delta_s = -I_p \rho_{\parallel s}/\Psi'_p$ .

### Appendix A.2. Magnetic differential equation for trapped particles

For trapped particles, the magnetic differential equation is given by

$$v_{\parallel} \hat{\mathbf{b}} \cdot \nabla \delta_s = \omega_s - \bar{\omega}_s. \quad (\text{A.8})$$

In coordinates  $\{\psi, \theta, \alpha\}$ , with  $\alpha = \zeta - q\theta$  (and  $\{\psi, \theta, \zeta\}$  being Boozer coordinates), one has

$$\omega_s = -\frac{1}{\tau_b \Psi'_p} [I_p \partial_{\theta} + (I_t - qI_p) \partial_{\alpha}] \rho_{\parallel s}, \quad (\text{A.9})$$

and equation (A.8) then reads

$$\tau_b^{-1} \partial_{\theta} \left( \frac{I_p}{\Psi'_p} \rho_{\parallel s} + \delta_s \right) = \tilde{\omega}_{s\alpha}, \quad (\text{A.10})$$

where

$$\tilde{\omega}_{s\alpha} := \frac{qI_p - I_t}{\Psi'_p} \left[ \tau_b^{-1} \partial_{\alpha} \rho_{\parallel s} - \overline{\tau_b^{-1} \partial_{\alpha} \rho_{\parallel s}} \right]. \quad (\text{A.11})$$

The coordinate along the magnetic field line,  $\theta$ , is not monotonic over the periodic orbit delimited by the bounce points  $\theta_{b1}$  and  $\theta_{b2}$ . We define a monotonic coordinate  $\tau$  by

$$\tau := \begin{cases} \int_{\theta_{b1}}^{\theta} |\tau_b| d\theta' & \text{when } \sigma > 0 \\ \hat{\tau}_b/2 - \int_{\theta_{b2}}^{\theta} |\tau_b| d\theta' & \text{when } \sigma < 0, \end{cases} \quad (\text{A.12})$$

with

$$\hat{\tau}_b = 2 \int_{\theta_{b1}}^{\theta_{b2}} |\tau_b| d\theta. \quad (\text{A.13})$$

Then, the solution of (A.10) can be easily written as

$$\delta_s = -\frac{I_p}{\Psi'_p} \rho_{\parallel s} + \int_0^{\tau} \tilde{\omega}_{s\alpha} d\tau'. \quad (\text{A.14})$$

In order to give a more explicit expression for (A.14), we use periodicity in  $\tau$  and write

$$\tilde{\omega}_{s\alpha} = \sum_{l \neq 0} (\omega_{s\alpha})_l e^{il\hat{\omega}_b \tau}, \quad (\text{A.15})$$

with  $\hat{\omega}_b := 2\pi/\hat{\tau}_b$  and

$$(\omega_{s\alpha})_l = (\hat{\tau}_b/2)^{-1} \int_0^{\hat{\tau}_b/2} \omega_{s\alpha}(\tau) \cos(l\hat{\omega}_b \tau) d\tau. \quad (\text{A.16})$$

Here, the fact that  $\omega_{s\alpha}(\tau)$  is even in  $\tau$  has been employed. Finally,

$$\delta_s = -\frac{I_p}{\Psi'_p} \rho_{\parallel s} + 2 \sum_{l>0} \frac{(\omega_{s\alpha})_l}{l \widehat{\omega}_b} \sin(l \widehat{\omega}_b \tau). \quad (\text{A.17})$$

Note that for axisymmetric tokamaks (A.17) simply gives  $\delta_s = -I_p \rho_{\parallel s} / \Psi'_p$ .

## Appendix B. Residual zonal flow with a source term in the quasineutrality equation

Figures B1 and B2 are analogous to figures 4 and 5, but this time we employ the equilibrium and parameters of Section 4, and show the results obtained by both CAS3D-K and GENE. The gyrokinetic simulations have been carried out by taking vanishing initial condition and adding a constant source term to the quasineutrality equation.

A formulation of the residual zonal flow problem similar to that given in [5, 6] gives, in the stellarator case,

$$\frac{\varphi_k(\infty)}{\varphi_k(0)} = \frac{\sum_s \frac{Z_s^2}{T_s} \{1 - J_{0s}^2\}_s}{\sum_s \frac{Z_s^2}{T_s} \left[ \{1\}_s - \left\{ e^{-ik_\psi \delta_s} J_{0s} \overline{e^{ik_\psi \delta_s} J_{0s}} \right\}_s^{\overline{\omega_s=0}} \right]}, \quad (\text{B.1})$$

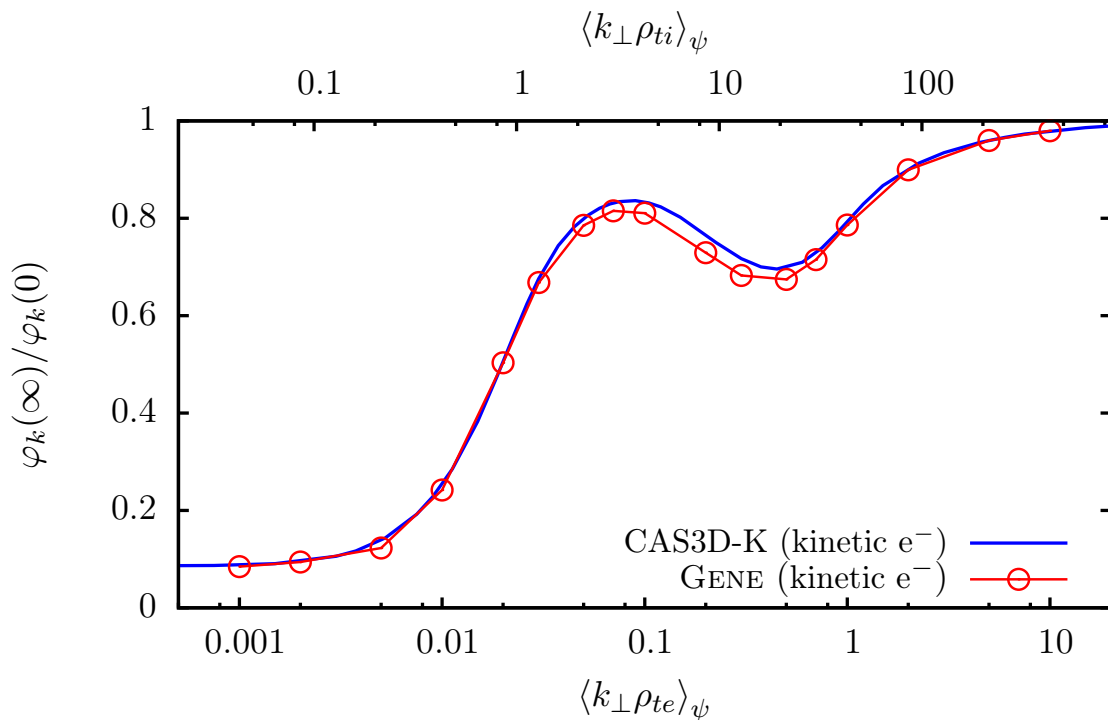


**Figure B1.** The evaluation of equation (50) with CAS3D-K for the tokamak of Section 4 at  $\psi = 0.25$  is shown. The corresponding simulation with GENE including a source term in the quasineutrality equation is also plotted.

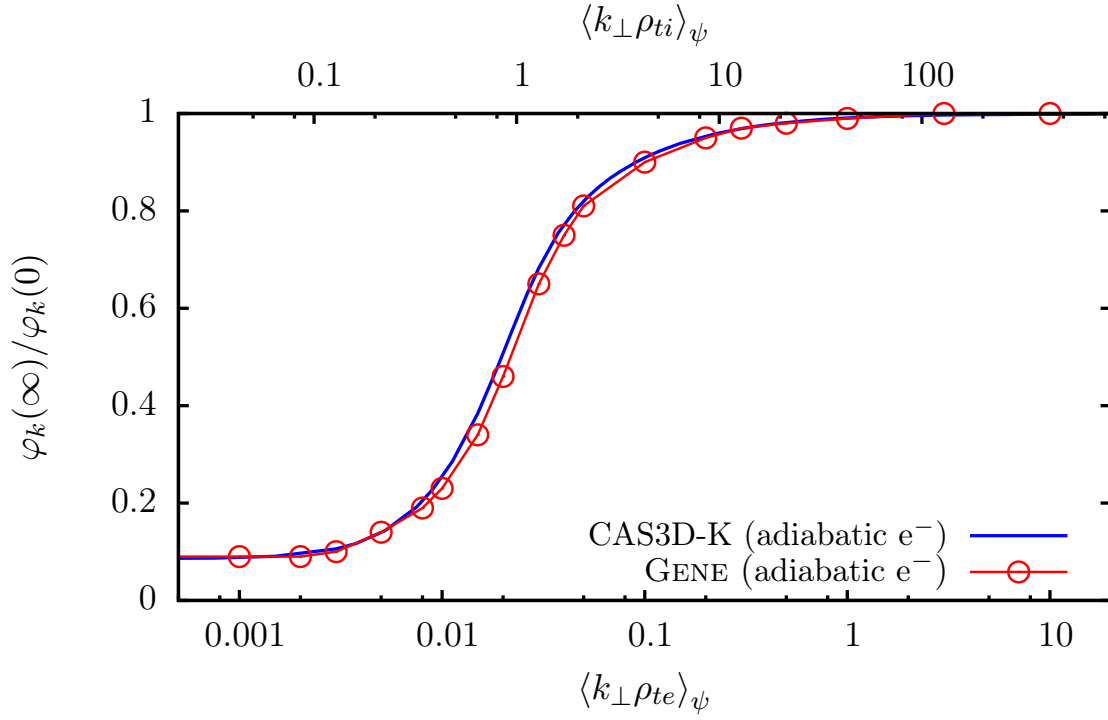


**Figure B2.** The same calculations as in figure B1, but employing adiabatic electrons.

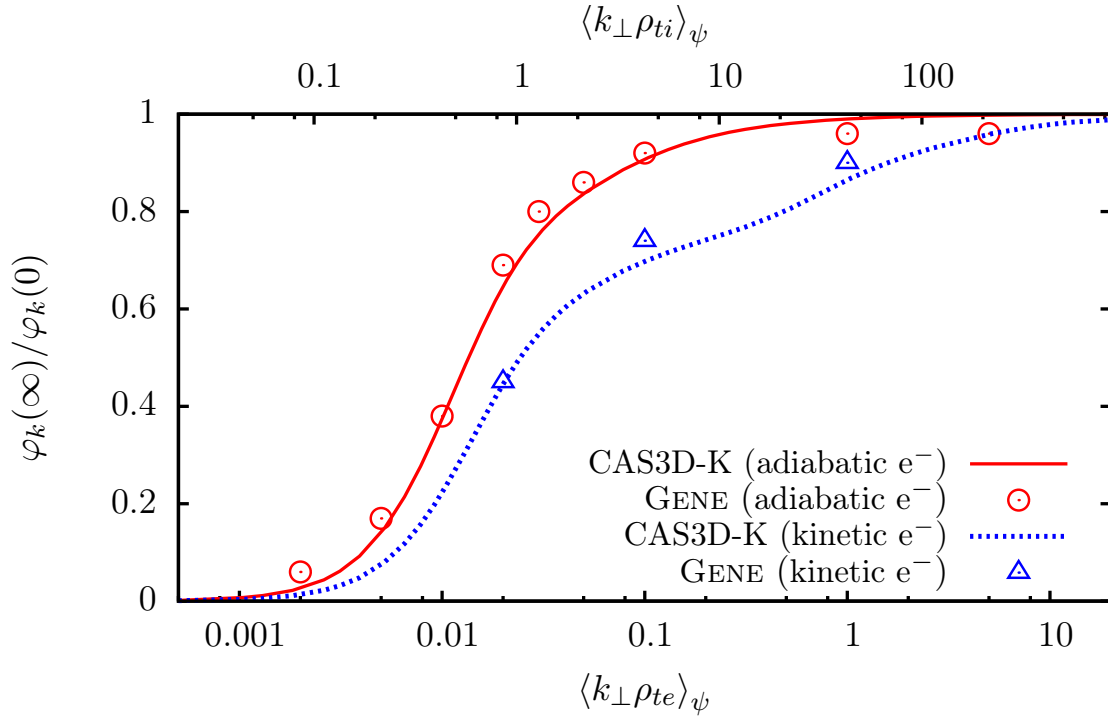


**Figure B3.** The results of the forced case for the standard configuration of the stellarator W7-X at  $\psi = 0.25$ .

if all species are kinetic. In the approximation of adiabatic electrons, one has

$$\frac{\varphi_k(\infty)}{\varphi_k(0)} = \frac{\sum_{s \neq e} \frac{Z_s^2}{T_s} \{1 - J_{0s}^2\}_s}{\sum_{s \neq e} \frac{Z_s^2}{T_s} \left[ \{1\}_s - \left\{ e^{-ik_{\psi} \delta_s} J_{0s} \overline{e^{ik_{\psi} \delta_s} J_{0s}} \right\}_s^{\overline{\omega_s=0}} \right]}. \quad (\text{B.2})$$

The evaluation of these expressions with CAS3D-K, for the standard configuration of the stellarator W7-X and the parameters detailed in Section 4, is shown in B3. The results for GENE simulations are also plotted.

## References

- [1] Hammett G W, Beer M A, Dorland W, Cowley S C and Smith S A 1993 *Plasma Phys. Control. Fusion* **35** 973
- [2] Diamond P H, Itoh S-I, Itoh K and Hahm T S 2005 *Plasma Phys. Control. Fusion* **47** R35-R161
- [3] Rosenbluth M N and Hinton F L 1998 *Phys. Rev. Lett.* **80** 724
- [4] Watanabe T-H, Sugama H and Ferrando-Margalet S 2008 *Phys. Rev. Lett.* **100** 195002
- [5] Xiao Y and Catto P J 2006 *Phys. Plasmas* **13** 102311
- [6] Xiao Y and Catto P J 2007 *Phys. Plasmas* **14** 055910
- [7] Sugama H and Watanabe T-H 2005 *Phys. Rev. Lett.* **94** 115001
- [8] Sugama H and Watanabe T-H 2006 *Phys. Plasmas* **13** 012501
- [9] Mishchenko A, Helander P and Könies A 2008 *Phys. Plasmas* **15** 072309
- [10] Helander P, Mishchenko A, Kleiber R and Xanthopoulos P 2011 *Plasma Phys. Control. Fusion* **53** 054006
- [11] Xanthopoulos P, Mishchenko A, Helander P, Sugama H and Watanabe T-H 2011 *Phys. Rev. Lett.* **107** 245002
- [12] Jenko F, Dorland W, Kotschenreuther M and Rogers B N 2000 *Phys. Plasmas* **7** 1904
- [13] Görler T, Lapillonne X, Brunner S, Dannert T, Jenko F, Merz F and Told D 2011 *J. Comput. Phys.* **230** 7053
- [14] The GENE code: <http://genecode.org>
- [15] Xanthopoulos P, Cooper W A, Jenko F, Turkin Yu, Runov A and Geiger J 2009 *Phys. Plasmas* **16** 082303
- [16] Jost G, Tran T M, Cooper W A, Villard L and Appert K 2001 *Phys. Plasmas* **8** 3321
- [17] Kleiber R and Hatzky R 2012 *Comput. Phys. Commun.* **183** 305
- [18] Catto P J 1978 *Plasma Phys. Control. Fusion* **20** 719
- [19] Frieman E A and Chen L 1982 *Phys. Fluids* **25** 502
- [20] Brizard A J and Hahm T S 2007 *Rev. Mod. Phys.* **79** 421
- [21] Parra F I and Calvo I 2011 *Plasma Phys. Control. Fusion* **53** 045001
- [22] Dubin D H E, Krommes J A, Oberman C and Lee W W 1983 *Phys. Fluids* **26** 3524
- [23] Parra F I and Barnes M 2015 *Plasma Phys. Control. Fusion* **57** 045002
- [24] Calvo I and Parra F I 2012 *Plasma Phys. Control. Fusion* **54** 115007
- [25] Parra F I and Barnes M 2015 *Plasma Phys. Control. Fusion* **57** 054003
- [26] Cary J R and Shasharina S G 1997 *Phys. Rev. Lett.* **78** 674
- [27] Cary J R and Shasharina S G 1997 *Phys. Plasmas* **4** 3323
- [28] Parra F I, Calvo I, Helander P and Landreman M 2015 *Nucl. Fusion* **55** 033005
- [29] Könies A 2000 *Phys. Plasmas* **7** 1139
- [30] Könies A, Mishchenko A and Hatzky R 2008 *AIP Conf. Proc., Theory of Fusion Plasmas* **1069** 133
- [31] Hirshman S P and Whitson J C 1983 *Phys. Fluids* **26** 3553
- [32] Yamagishi O and Sugama H 2012 *Phys. Plasmas* **19** 092504
- [33] Nunami M, Watanabe T-H and Sugama H 2010 *Plasma and Fusion Res.* **5** 016
- [34] The HYDRA supercomputer: <http://www.mpcdf.mpg.de/services/computing/hydra/about-the-system>
- [35] The MareNostrum III: <http://www.bsc.es/marenostrum-support-services/mn3>